

Micronekton distribution as influenced by mesoscale eddies, Madagascar shelf and shallow seamounts in the south-western Indian Ocean: An acoustic approach

Annasawmy Pavanee ^{1,2,*}, Ternon Jean-Francois ¹, Lebourges-Dhaussy Anne ³, Roudaut Gildas ³, Cotel Pascal ¹, Herbette Steven ⁴, Ménard Frédéric ⁵, Marsac Francis ^{1,2}

¹ MARBEC, Univ. Montpellier, CNRS, Ifremer, IRD, Sète, France

² Department of Biological Sciences and Marine Research Institute/ICEMASA, University of Cape Town, Cape Town, South Africa

³ LEMAR, IRD, UBO, CNRS, Ifremer, Plouzané, France

⁴ Laboratoire d'Océanographie Physique et Spatiale (LOPS), IUEM, Univ. Brest, CNRS, Ifremer, IRD, Brest, France

⁵ Aix Marseille Univ., Université de Toulon, CNRS, IRD, MIO, Marseille, France

* Corresponding author : Pavanee Annasawmy, email address : angelee-pavanee.annasawmy@ird.fr

Abstract :

An investigation of the vertical and horizontal distributions of micronekton, as influenced by mesoscale eddies, the Madagascar shelf and shallow seamounts, was undertaken using acoustic data collected during two research cruises at an unnamed pinnacle (summit depth ~240 m) thereafter named "MAD-Ridge", and at La Pérouse seamount (~60 m) in the south-western Indian Ocean. MAD-Ridge is located to the south of Madagascar, in an "eddy corridor", known both for its high mesoscale activity and high primary productivity. In contrast, La Pérouse is located on the outskirts of the Indian South Subtropical Gyre (ISSG) province, characterised by low mesoscale activity and low primary productivity. During the MAD-Ridge cruise, a dipole was located in the vicinity of the seamount, with the anticyclone being almost stationary on the pinnacle. Total micronekton acoustic densities were greater at MAD-Ridge than at La Pérouse. Micronekton acoustic densities of the total water column were lower within the anticyclone than within the cyclone during MAD-Ridge. Micronekton followed the usual diel vertical migration (DVM) pattern, except within the cyclone during MAD-Ridge where greater acoustic densities were recorded in the daytime surface layer. The backscatter intensities were stronger at the 38 kHz than at the 70 and 120 kHz frequencies in the daytime surface layer at MAD-Ridge cyclonic stations. These backscatter intensities likely correspond to gas-filled swimbladders of epi- and mesopelagic fish actively swimming and feeding within the cyclone or gelatinous organisms with gas inclusions. Our findings evidenced that the distributions of micronekton and DVM patterns are complex and are influenced significantly by physical processes within mesoscale eddies. The mesoscale eddies' effects were dominant over any potential seamount effects at the highly dynamic environment prevailing at MAD-Ridge during the cruise. No significant increase in total micronekton acoustic densities was observed over either seamount, but dense aggregations of biological scatterers were observed on their summits during both day and night.

Keywords : Micronekton, Diel vertical migration, Mesoscale eddies, Madagascar shelf, Seamount, South-western indian ocean

28 1. Introduction

29 Features such as mesoscale cyclonic and anticyclonic eddies, upwelling events, tidal fronts,
30 shelves, seamounts and river runoff play a significant role in regional ecosystems (Bakun,
31 2006; Mann and Lazier, 2006; Benitez-Nelson and McGillicuddy, 2008). Mesoscale cyclonic
32 and anticyclonic eddies are ubiquitous in the world's oceans (Chelton et al., 2011). They have
33 time-scales of approximately 10-30 days and horizontal scales between 10 and 100 km
34 (Mann and Lazier, 2006; Chelton et al., 2011). In oligotrophic systems, eddies are important
35 features because they provide mechanisms whereby the physical energy of the ocean is
36 converted to trophic energy to support biological processes (Bakun, 2006; Godø et al., 2012).
37 Cyclonic eddies, through upwelling of nutrients in their centres from deeper layers to the
38 euphotic zone, are usually known to enhance local productivity (Owen, 1980, 1981;
39 McGillicuddy and Robinson, 1997; McGillicuddy et al., 1998; Klein and Lapeyre, 2009;
40 Huggett, 2014; Singh et al., 2015). Anticyclonic eddies may promote the development of
41 frontal structures (Bakun, 2006). In anticyclones, highly productive waters may be entrained
42 laterally from nearby regions to the eddy periphery or upwelling of nutrients may occur along
43 the eddy boundary (McGillicuddy, 2016). At the frontier between eddies, smaller-scale or
44 submesoscale features (elongated filaments with a 10-km width) have been reported to
45 enhance nutrient supply and primary productivity in oligotrophic conditions (Lévy et al.,
46 2001, 2018; Klein and Lapeyre, 2009). Biological responses to eddies, however, are complex
47 and depend on a range of factors including seasonal modulation of the mixed layer depth
48 (Dufois et al., 2014), timing, magnitude and duration of nutrient input and also on eddy
49 properties such as the formation, intensity, age and eddy-induced Ekman pumping (Benitez-
50 Nelson and McGillicuddy, 2008).

51 Continental shelves and seamounts are also features that may lead to enhanced productivity
52 when certain conditions are met. Upwelling regions south of Madagascar have been observed

53 to be biological hotspots with increased productivity (Raj et al., 2010; Ramanantsoa et al.,
54 2018) and increased acoustic biomass estimates of pelagic fish and whale sightings (Pripp et
55 al., 2014). Phytoplankton types may also differ between continental shelves and ocean basins,
56 with shelf areas exhibiting larger phytoplankton cells because of the processes leading to high
57 nutrient concentrations in the euphotic zone and cells rapidly take up nutrients (Nishino et al.,
58 2011). Seamounts are ubiquitous features of the world's oceans and have been reported to
59 influence the prevailing ocean currents (Royer, 1978; White et al., 2007), creating various
60 local dynamic responses such as formation of a Taylor column, isopycnal doming (Mohn and
61 Beckmann, 2002), enclosed circulation cell (White et al., 2007), upwelling, vertical mixing of
62 nutrient-rich waters and enhanced productivity (Boehlert and Genin, 1987; Genin, 2004). In a
63 nutrient-limited environment like the south-western Indian Ocean, processes injecting
64 nutrients into the euphotic zone (such as mesoscale features, seamounts, coastal upwelling
65 events and river runoff) are likely to modulate the chlorophyll *a* signature by increasing
66 phytoplankton growth, attracting a range of secondary and tertiary consumers such as
67 zooplankton and micronekton.

68 Mesopelagic micronekton are actively swimming organisms that typically range in size from
69 2 to 20 cm. They include diverse taxonomic groups (De Forest and Drazen 2009) such as
70 crustaceans (adult euphausiids, pelagic decapods and mysids), cephalopods (small species
71 and juvenile stages of large oceanic species) and fish (mainly mesopelagic species and
72 juveniles of other fish) (Brodeur et al., 2005; Brodeur and Yamamura 2005; Ménard et al.,
73 2014). Gelatinous organisms are under-represented components of the mesopelagic
74 community (Lehodey et al., 2010; Kloser et al., 2016). Micronekton are important in the
75 energy transfer to higher trophic levels because they are preyed upon by various top marine
76 predators (Guinet et al., 1996; Bertrand et al., 2002; Potier et al., 2007; Cherel et al., 2010;
77 Danckwerts et al., 2014; Jaquemet et al., 2014). They also transport energy to deeper regions
78 of the ocean via respiration, excretion and natural mortality (Hidaka et al., 2001; Catul et al.,

79 2011; Bianchi et al., 2013). This energy transport is made possible by the extensive diel
80 vertical migration (DVM) patterns of some micronekton species, with the organisms
81 migrating to the upper 200 m of the water column at dusk and below 400 m at dawn
82 (Lebourges-Dhaussy et al., 2000; Béhagle et al., 2014; Annasawmy et al., 2018). Diel vertical
83 migration is believed to result from a compromise between the need to feed and to avoid
84 predation (Heywood, 1996), with light being the main controlling factor in initiating ascent
85 and descent (Heywood, 1996; Andersen et al., 1998; Brierley, 2014). The distribution of
86 micronekton communities across ocean basins is not uniform (Judkins and Haedrich, 2018).
87 Some studies have reported higher biomasses of micronekton scattering layers at seamount
88 flanks and summits relative to the surrounding ocean, e.g. the Emperor (265m, Boehlert,
89 1988) and Cross seamounts in the Pacific (330 m, Johnston et al., 2008); Condor (182-214 m)
90 and Gigante (161 m) seamounts in the Azores (Cascão et al., 2017).

91 At the ocean-basin scale, the western side of the oligotrophic Indian South Subtropical Gyre
92 (ISSG) biogeochemical province (Longhurst, 2007) holds reduced micronekton abundances
93 and acoustic densities relative to the dynamic and more productive East African Coastal
94 (EAFC) province (Annasawmy et al., 2018). Within the ISSG and EAFC provinces, features
95 such as eddies, coastal upwelling at the Madagascar shelf and seamounts may further impact
96 the local productivity, resulting in significant variability in micronekton distributions via
97 bottom-up processes. This paper investigates the influence of mesoscale eddies, the South
98 Madagascar shelf and two shallow seamounts, La Pérouse and an unnamed pinnacle on the
99 Madagascar Ridge, hereafter called “MAD-Ridge”, in shaping micronekton vertical and
100 horizontal distributions by combining data from ship-based platforms (acoustics, current
101 profiler and CTD) and satellite altimetry.

102

103 **2. Material and Methods**

104 2.1 Cruises

105 Two research surveys were carried out on board the RV *Antea* at La Pérouse (19°43'S and
106 54°10'E) and MAD-Ridge seamounts (27°29'S and 46°16'E). La Pérouse (summit depth ~60
107 m) is located along the north-western boundary of the ISSG province and MAD-Ridge
108 (summit depth ~240 m) is located on the southern boundary of the EAFR (Fig. 1a). The La
109 Pérouse cruise (DOI: 10.17600/16004500) investigated the area within 10-18 km around the
110 seamount from the 15 to 30 September 2016 (Fig. 1b). The MAD-Ridge Leg 1 cruise (DOI:
111 10.17600/16004800) was divided into a West-East transect (248 km long from hydrographic
112 station 1 to 15) and a South-North transect (292 km long from hydrographic station 16 to 31)
113 and took place from the 8 to 24 November 2016 (Fig. 2).

114 2.2 Satellite data

115 The mesoscale eddy field during both the La Pérouse and MAD-Ridge cruises were described
116 using daily delayed-time Absolute Dynamic Topography (ADT) with 1/4° (~25 km) spatial
117 resolution. Delayed-time ADT was produced and distributed by the Copernicus Marine
118 Environment Monitoring Service project (CMEMS) and available at
119 <http://marine.copernicus.eu/>, from which absolute geostrophic currents have been calculated
120 and used to derive dynamic parameters (see next section). Delayed-time Mean Sea Level
121 Anomalies (MSLA) data, with 1/4° (~25 km) spatial resolution in the vicinity of MAD-Ridge
122 seamount were also downloaded from <http://marine.copernicus.eu/>, and used for direct eddy
123 field representation.

124 2.3 Field sampling

125 2.3.1 *In situ* bathymetry

126 The 12 kHz frequency of a Simrad EA500 echosounder was used to acquire a detailed
127 bathymetry of the seamounts. The bathymetry data were interpolated on a regular grid using
128 the Golden Surfer © software (version 10.3.705).

129 2.3.2 Hydrographic stations

130 A Sea-Bird 911+ CTD rosette system equipped with a Wetlabs ECO FL fluorometer was
131 used to profile temperature, fluorescence and dissolved oxygen from the surface to a depth of
132 ~1000 m during the La Pérouse and MAD-Ridge cruises. Discrete samples of chlorophyll *a*
133 measured by high pressure liquid chromatography was used to calibrate the fluorescence
134 sensor of the CTD during both cruises and to determine the depth range where the maximum
135 chlorophyll *a* values (F_{max}) were found. The integrated chlorophyll *a* concentrations
136 between 2 and 200 m (mg m^{-3}) was calculated by taking the sum of chlorophyll *a* values in
137 that depth range. The average depths of the thermocline were assessed from the CTD profiles
138 using the 20°C isotherm depth as a proxy.

139 Two 300 kHz RDI (upward and downward-looking) L-ADCP current profilers attached to the
140 CTD frame were used to investigate the vertical structure of the current field during both
141 cruises. The S-ADCP data were collected with a 75 kHz RDI Ocean Surveyor II. As L-ADCP
142 data were missing at MAD-Ridge stations 2 and 3, S-ADCP data were used instead. The L-
143 ADCP data were collected to a depth of 1000 m whereas the S-ADCP data were collected to
144 a depth of 600 m. Both datasets showed strong correlations which allowed the use of the L-
145 with the S-ADCP (Vianello et al., 2020). For each hydrographic station, the average current
146 speed (in cm s^{-1}) over the depth range 104-304 m, was calculated from the west-east zonal
147 (u) and south-north meridional (v) velocity components measured by the S-ADCP or L-
148 ADCP.

149 A classification of MAD-Ridge hydrographic stations (numbered 1-31, Fig. 2) was performed
150 based on their location relative to the mesoscale eddies (cyclonic, anticyclonic, interface

151 between the dipole), to the seamount (summit or flank, both within the anticyclonic eddy) and
 152 to the Madagascar shelf. This classification was based on the hydrology (temperature-salinity
 153 profiles) of each station and a standard dynamical parameter, the Okubo-Weiss parameter, W
 154 (Okubo, 1970; Weiss, 1991; Isern-Fontanet et al., 2004). The latter is calculated from
 155 equation 1 below, where S_n is the normal strain, S_s the shear strain, ω the relative vorticity,
 156 and u and v (Eq. 2 below) are the surface geostrophic velocity zonal and meridional
 157 components derived from the absolute dynamic topography (altimetry). The Okubo-Weiss
 158 parameter allows the separation of the flow into a vorticity-dominated region ($W < -W_0$) and
 159 a strain-dominated region ($W > -W_0$), with $W_0 = 0.2\sigma_w$, (σ_w being the standard deviation of
 160 W over the whole domain) (Isern-Fontanet et al., 2004). It has been used widely in the south-
 161 western Indian Ocean by Halo et al. (2014) to distinguish the core of eddies ($W > -W_0$) from
 162 the periphery of eddies ($W < -W_0$) and is given by:

$$163 \quad W = S_n^2 + S_s^2 - \omega^2 \quad \text{Eq. 1,}$$

164 where:

$$165 \quad S_n = \frac{\partial u}{\partial x} - \frac{\partial v}{\partial y}, \quad S_s = \frac{\partial v}{\partial x} + \frac{\partial u}{\partial y}, \quad \omega = \frac{\partial v}{\partial x} - \frac{\partial u}{\partial y} \quad \text{Eq. 2}$$

166 However, W values have to be used cautiously against *in situ* data because the spatial
 167 resolution of the altimetry is low (~25 km) relative to each station. Therefore, for each
 168 station, the altimetry data were complemented by the available *in situ* data such as sea surface
 169 temperature and salinity obtained from a ship-mounted thermosalinograph and dissolved
 170 oxygen obtained from the CTD. This combined set of information allowed us to segregate the
 171 stations into different categories (see example for stations 3, 5 and 13, Supplementary
 172 Material, Fig. 1 and Supplementary Material, Table 1).

173 2.3.3 Zooplankton sampling

174 Daytime zooplankton samples were collected with a 200- μ m-mesh oblique Bongo net towed
175 at a speed of 1-2 knots to a maximum depth of 200 m during the La Pérouse cruise (0.28 m²
176 mouth area). A 200- μ m-mesh oblique Multinet was towed to a maximum of 200 m during the
177 MAD-Ridge cruise (0.25 m² mouth area) (Noyon et al., 2020). Samples from both cruises
178 were emptied into a 200 μ m sieve, poured into sampling jars with filtered seawater and stored
179 in 4% buffered formaldehyde at room temperature on board before being analysed using a
180 Hydroptic Zooscan following the protocols in Gorsky et al. (2010). Detailed zooplankton
181 sampling and analyses were investigated in Noyon et al. (2020).

182 2.3.4 Acoustic sampling

183 A Simrad EK60 echosounder operating at four frequencies was used during both the La
184 Pérouse and Leg 1 of the MAD-Ridge cruises: 38 kHz at 1000 W transmitted power, 70 kHz
185 (acquired range of 500 m) at 750 W, 120 kHz (250 m) at 200 W and 200 kHz (150 m) at 90
186 W. The water column was correctly sampled to a depth of 735 m during data acquisition for
187 the 38 kHz frequency of the La Pérouse cruise, with data being of poor quality below that
188 depth. For comparison with the La Pérouse cruise, echo-integrated acoustic data for the 38
189 kHz frequency of the MAD-Ridge cruise has also been selected down to 735 m in this study.
190 The pulse duration was set at 0.512 ms. The transducers were calibrated prior to both cruises
191 following the procedures recommended in Foote et al. (1987). MAD-Ridge acoustic data
192 were collected along the West-East and South-North transects (Fig. 2) at a vessel speed of 8-9
193 knots. Additional transects were also conducted during the day and night in close proximity
194 to the MAD-Ridge summit and flanks at vessel speeds of 8-9 knots (Supplementary Material,
195 Fig. 2).

196 The Matecho software (an open source IRD tool computed with MATLAB 7.11.0.184,
197 Release 2010b- and based on the IFREMER's Movies3D software; Trenkel et al., 2009;
198 Perrot et al., 2018) was used to process and visualize acoustic data from both cruises.

199 Background, transient and impulsive noises along with attenuated signals (Perrot et al., 2018)
200 were removed using the algorithms designed in De Robertis and Higginbottom (2007) and
201 Ryan et al. (2015). An offset of 10 m below the sea surface was applied to account for the
202 acoustic detection of the surface turbulence. During both cruises, echo-integration of the
203 acoustic data was performed on 1-m layers at an elementary sampling distance unit of 0.1
204 nmi (nautical mile) and at a threshold of -80 dB to exclude scatterers (entities contributing to
205 the backscattered energy) not representative of the micronekton community (Béhagle et al.,
206 2017). The micronekton acoustic density was determined by the nautical area scattering
207 coefficient NASC (s_A , $m^2 \text{ nmi}^{-2}$), related to the backscattered energy (MacLennan et al.,
208 2002). NASC can be used as a proxy of the relative biomass of micronekton provided
209 assumptions that the composition of scattering layers and the resulting scattering properties of
210 micronekton are relatively homogeneous (Béhagle et al., 2014). The volume backscattering
211 strength (S_V , dB re 1 m^{-1} ; MacLennan et al., 2002) was also calculated for each frequency (38
212 kHz, 70 kHz and 120 kHz) to obtain the relative acoustic density of scatterers per unit
213 volume and was used to generate Red Green Blue (RGB) composite images (see next
214 section). The water column at the 38 kHz frequency was separated into the following depth
215 categories, based on epipelagic and mesopelagic layers: surface (10-200 m), intermediate
216 (200-400 m), deep (400-735 m) and total water column (10-735 m). Diurnal and nocturnal
217 periods were assessed using Matecho software through visual analysis of the echograms.

218 2.4 Data visualisation

219 Vertical distributions of the environmental descriptors (current speed, temperature and
220 chlorophyll *a*) were mapped from the surface to ~1000 m (except for chlorophyll) along the
221 west-east and south-north transects of MAD-Ridge Leg 1 (Fig. 3a, b) using the Section mode
222 of the software Ocean Data View (ODV, version 4.5.7; Schlitzer, 2013). The chlorophyll *a*
223 data were only mapped from the surface to 300 m because values were below the minimum

224 level of detection deeper than that (Fig. 3c). Data interpolation between sampling stations
225 was carried out using the DIVA (Data-Interpolating Variational Analysis) gridding option in
226 ODV that spatially interpolates observations on a regular grid in an optimal way by taking
227 into account coastlines and bathymetric features to structure and divide the domain on which
228 estimations are performed.

229 Acoustic data were represented using RGB colour coding. RGB composite images were
230 generated in MATLAB (version 2016) based on the 38 kHz, 70 kHz and 120 kHz echo-
231 integrated acoustic data of selected transects during the MAD-Ridge and La Pérouse cruises.
232 The 38, 70 and 120 kHz echo-integrated acoustic data were given in red, green and blue
233 colour codes respectively on each RGB plot, with the dynamic of the S_v values in dB for
234 each frequency being converted in 256 (0-255) levels of each colour. A linear transformation
235 of the backscatter was applied to each frequency (fr):

$$236 \text{ Colour index (fr)} = [255 / (\text{High scale threshold} - \text{Low scale threshold})] \times [S_v(\text{fr}) - \text{Low scale} \\ 237 \text{ threshold}], \quad \text{Eq. 3}$$

238 where the high and low scale thresholds are the maximum and minimum backscatter for hue
239 visualisations, respectively. $S_v(\text{fr})$ is the backscatter value at each frequency. This acoustic
240 visualisation technique is useful in determining the relative contribution of each frequency to
241 the overall backscatter (red means that S_v 38 is dominant, and similarly for green and blue,
242 S_v 70 and S_v 120 are respectively dominant) and to identify dense aggregations of scatterers
243 (S_v 38, S_v 70 and S_v 120 all dominant and seen as “white patches”). On a RGB composite
244 image based on the 38, 70 and 120 kHz frequencies, a dark red colour indicates a dominant
245 but low 38 kHz backscatter, whereas a light red colour indicates a dominant but high 38 kHz
246 backscatter. The same rule applies to the green (70 kHz) and blue (120 kHz) hues. Kloser et
247 al. (2002) used a similar approach, but the composite image was produced by assigning a

248 separate colour palette to each frequency (12, 38 and 120 kHz) and dynamically optimising
249 the frequencies to highlight the amplitude differences in the echogram.

250 2.5 Statistical analyses

251 Kruskal Wallis tests and pairwise Wilcoxon rank sum tests were performed to assess the
252 differences in integrated chlorophyll *a* concentrations between classified hydrographic
253 stations. In order to cover the largest depth range, day and night acoustic transects at 38 kHz
254 frequency were further selected to investigate the micronekton acoustic densities in close
255 proximity to the summits and flanks of the pinnacles (see Supplementary Material Fig. 2). As
256 the 38 kHz frequency data did not follow a normal distribution, non-parametric Wilcoxon
257 rank sum tests were performed to compare the overall acoustic densities in each of the depth
258 categories (surface, intermediate and deep) between La Pérouse and MAD-Ridge seamounts,
259 and between day and night. Daytime acoustic density estimates representing the vertical
260 distribution of micronekton across the depth categories (surface: 10-200 m; intermediate:
261 200-400 m; deep: 400-735 m; total water column: 10-735 m) and averaged over 0.4 nmi on
262 each side of the classified stations during MAD-Ridge cruise were investigated using non-
263 parametric Kruskal-Wallis (KW) tests and pairwise Wilcoxon rank sum tests. All statistical
264 tests were performed with version 3.3.1 of the R package.

265 2.6 Taylor column theoretical calculation

266 The following non-dimensional factors were used to determine the likelihood of a Taylor
267 column formation over La Pérouse and MAD-Ridge summits (White et al., 2007), depending
268 on the mean water stratification, the mean flow field, the latitude (earth's rotation effect) and
269 the shape of the seamount:

270 (1) The Rossby number, Ro , with $Ro = \frac{U}{f \times L}$,

271 where U is the typical flow speed (0.3 m s^{-1} at La Pérouse and 0.5 m s^{-1} at MAD-Ridge);
 272 $f = 2 * \Omega * \sin(\textit{latitude})$, where Ω is Earth's angular velocity at $0.0000729 \text{ rads s}^{-1}$; the
 273 $\sin(\textit{latitude})$ is $\sin(19.72)$ at La Pérouse and $\sin(27.48)$ at MAD-Ridge; and L is the
 274 average width of the seamounts ($10\,000 \text{ m}$ for La Pérouse and $27\,500 \text{ m}$ for MAD-Ridge). Ro
 275 estimates were calculated at 0.27 at La Pérouse and 0.17 at MAD-Ridge.

276 (2) The relative height of the seamount (h_0) to water depth (H), with $\alpha = \frac{h_0}{H}$,

277 where α was calculated at 0.99 at La Pérouse and 0.85 at MAD-Ridge.

278 (3) A combination of Ro and α gives the blocking parameter Bl (where $Bl = \frac{\alpha}{Ro}$),

279 which controls the formation of a Taylor column (White et al., 2007). A Bl value of 3.66 was
 280 calculated at La Pérouse and 4.88 at MAD-Ridge. According to Chapman and Haidvogel
 281 (1992), for seamounts taller than $\alpha \approx 0.4$, true Taylor caps will form if $Ro < 0.15$ and $Bl > \sim 2$
 282 for Gaussian-shaped seamounts with moderate stratification. According to the authors, Taylor
 283 cones will not form if the Rossby number exceeds the upper bound of 0.15 - 0.2 .

284

285 3. Results

286 3.1 Synoptic ocean circulation during the MAD-Ridge cruise

287 A cyclonic/anticyclonic eddy dipole was encountered along the West-East transect
 288 (hydrographic stations 1-15) of Leg 1 of the MAD-Ridge cruise, whereas the South-North
 289 transect (hydrographic stations 16-31) was mostly located inside the anticyclonic eddy and
 290 reached the Madagascar shelf (Fig. 2). Along the West-East transect, at hydrographic station
 291 5, a sharp front was observed in the sea surface temperature and salinity data collected from
 292 the ship-mounted thermosalinograph, indicating the transition between cyclonic and
 293 anticyclonic circulations (Supplementary Material, Fig. 1). This transition area coincided
 294 with the largest current velocity recorded at the surface (158 cm s^{-1}) and in the depth layer

295 104 and 304 m (99 cm s^{-1}) relative to all other stations along the West-East and South-North
296 transects (Fig. 3a).

297 MAD-Ridge hydrographic stations were divided into six categories, according to whether
298 they belonged to the cyclonic eddy (C: stations 2, 3, 4), anticyclonic eddy (AC: stations 10-
299 13, 16-19, 24, 25), dipole interface (Dipole I: station 5), seamount summit and anticyclonic
300 eddy (Summit/AC: stations 8, 21, 22), seamount flank and anticyclonic eddy (Flank/AC:
301 stations 7, 9, 20, 23) and shelf (Shelf: stations 30, 31). The other hydrographic stations 1, 6,
302 14, 15, 26-29 could not be accurately resolved using the criteria mentioned in Section 2.3.1
303 and Supplementary Material Fig. 1, and were not assigned to any of the listed categories.

304 3.2 Hydrography and chlorophyll concentration during the MAD-Ridge cruise

305 Surface temperatures among the station categories varied between 23.7°C (cyclonic station 4)
306 and 24.9°C (Summit/AC station 21). The cyclonic and shelf stations were characterised by a
307 shallower thermocline (79-165 m and 97-117 m, respectively) than the anticyclonic stations.
308 The anticyclonic, Summit/AC and Flank/AC stations were characterised by a relatively
309 deeper thermocline (159-219 m, 206-209 m and 181-212 m, respectively) (Fig. 3b). F_{max}
310 values of $0.35\text{-}0.38 \text{ mg m}^{-3}$ and $0.62\text{-}0.74 \text{ mg m}^{-3}$ were recorded at the cyclonic and shelf
311 stations respectively, at depths of 54-122 m and 56-73 m, respectively (Fig. 3c). The
312 anticyclonic, Summit/AC and Flank/AC stations had deeper F_{max} depths (82-129 m, 131-
313 153 m and 101-144 m) relative to the cyclonic and shelf stations, with F_{max} values of 0.16-
314 0.30 mg m^{-3} , $0.25\text{-}0.31 \text{ mg m}^{-3}$ and $0.17\text{-}0.33 \text{ mg m}^{-3}$, respectively. Integrated chlorophyll *a*
315 concentrations were statistically different between the classified hydrographic stations (KW,
316 $H=7.59$, $p < 0.05$), especially between the cyclonic and anticyclonic stations (pairwise
317 comparisons, $p < 0.05$). The mean \pm S.D (standard deviation) integrated chlorophyll *a*
318 concentrations between 2 and 200 m were estimated at $29.1 \pm 7.3 \text{ mg m}^{-3}$ and $19.3 \pm 2.1 \text{ mg}$
319 m^{-3} within the cyclonic and anticyclonic eddies respectively.

320 3.3 Micronekton acoustic densities at the MAD-Ridge seamount

321 West-East Transect

322 The daytime total micronekton acoustic densities of the 38 kHz echosounder frequency
323 exhibited a decreasing trend along the West-East transect, with the greatest responses
324 recorded across stations 1-2 within the cyclonic eddy during Day_I (Fig. 4, Supplementary
325 Material Table 2). The lowest acoustic responses were recorded across the Summit/AC
326 station 8 during Day_III and stations 13-15 at the eastern periphery of the anticyclonic
327 circulation during Day_V. The night-time total micronekton acoustic densities were greater
328 than the daytime acoustic responses and also exhibited a decreasing trend along the West-
329 East transect. The greatest acoustic densities were recorded during Night_I between cyclonic
330 stations 3 and 4 and the lowest densities were recorded during Night_IV between stations 12
331 and 13 at the anticyclonic periphery (Fig. 4). Differences of $1536 \text{ m}^2 \text{ nmi}^{-2}$, $1297 \text{ m}^2 \text{ nmi}^{-2}$,
332 $1058 \text{ m}^2 \text{ nmi}^{-2}$ and $595 \text{ m}^2 \text{ nmi}^{-2}$ in the micronekton acoustic responses were recorded
333 between Night_I-Day_I, Night_II-Day_II, Night_III-Day_III and Night_IV-Day_IV,
334 respectively. Interestingly, the surface layer gathered higher percentage acoustic densities
335 than the deep layer during Day_I (stations 1-2), Day_II (Stations 4-6) and Day_III (stations
336 7-9), whereas the deep layer showed greater percentage acoustic densities than the surface
337 layer during Day_IV and Day_V (Fig. 4). The surface layer at night displayed greater
338 acoustic densities than the deep layer from Night_I to Night_IV (Fig. 4, Supplementary
339 Material Table 2). The intermediate layer displayed the lowest percentage acoustic responses
340 (1-10%) during day and night.

341 The echogram of the 38 kHz frequency showed organisms aggregating on the summits of
342 deep topographic features labelled X and Y between 300 and 500 m and on the MAD-Ridge
343 summit (Fig. 5). These organisms contributed to the higher acoustic densities within the
344 intermediate layer at Night_II relative to the intermediate layer across other transects. This

345 echogram also provided evidence of organisms migrating to deeper layers (below 400 m) at
346 sunrise and forming a dense aggregation between 400 and 600 m between the deep
347 topographic feature Y and MAD-Ridge seamount (Fig. 5). Micronekton assemblages at the
348 MAD-Ridge summit has been investigated in more detail in Annasawmy et al. (2019) and
349 Cherel et al. (2020).

350 RGB composite images showed a dominant and strong 38 kHz backscatter (red colour
351 dominating RGB plot) between ~20 and 70 m across the cyclonic stations 2 and 3 during
352 daytime and between ~20 and 120 m across the cyclonic stations 3 and 4 during night time
353 and sunrise (Fig. 6). Between the anticyclonic stations 10 to 12 and across stations 13 and 15,
354 the backscatter of the 38 kHz frequency was dominant but lower between ~20 and 80 m
355 compared to the cyclonic stations. At these anticyclonic stations, the dominant and stronger
356 120 kHz backscatter between ~80 and 140 m during daytime matches the Fmax depth of 82
357 and 129 m.

358 South-North transect

359 The total daytime acoustic densities of the 38 kHz echosounder frequency across the South-
360 North transect were greater during Day_VI at the southern boundary of the anticyclone,
361 decreased during Day_VII and Day_VIII along the summit/flanks and within the anticyclone,
362 before increasing at the northern periphery of the anticyclone during Day_IX and at the shelf
363 station 30 during Day_X (Fig. 7, Supplementary Material Table 3). The night time acoustic
364 responses followed the same pattern as the daytime acoustic densities along the South-North
365 transect, with the greatest responses across Night_VI at the southern periphery of the
366 anticyclone and Night_IX at its northern boundary (Supplementary Material, Table 3). The
367 lowest responses along the South-North transect were recorded across Night_VII and
368 Night_VIII over the summit and within the anticyclone. Differences of $1559 \text{ m}^2 \text{ nmi}^{-2}$, 1132
369 $\text{m}^2 \text{ nmi}^{-2}$, $1071 \text{ m}^2 \text{ nmi}^{-2}$ and $1719 \text{ m}^2 \text{ nmi}^{-2}$ in the micronekton acoustic densities were

Journal Pre-proof

370 recorded between Night_VI-Day_VI, Night_VII-Day_VII, Night_VIII-Day_VIII and
371 Night_IX-Day_IX respectively. In contrast with Day_I, Day_II and Day_III along the West-
372 East transect, the percentage micronekton acoustic responses at the 38 kHz echosounder
373 frequency in the surface layer during the day was lower than that in the deep layer across all
374 stations, except at the summit station during Day_VIII (Fig. 7). Across Night_VI to
375 Night_IX, the surface layer gathered greater micronekton acoustic responses compared to the
376 deep layer (Fig. 7, Supplementary Material, Table 3). Similar to the West-East transect, the
377 intermediate layer along the South-North transect gathered the lowest percentage
378 micronekton acoustic responses (4-11%) both during the day and night.

379 RGB composite images showed a dominant and relatively high 38 kHz backscatter between
380 ~20-100 m across stations 21, 22, 23 (on the summit and flank, within the anticyclone) and
381 shelf stations 30 and 31 (Fig. 8). The 120 kHz backscatter was dominant between ~100 and
382 140 m, corresponding with Fmax depths ranging from 116 to 138 m at these stations. Across
383 the shelf, the 120 kHz backscatter was dominant between 60 and 80 m, corresponding to
384 Fmax depths of 56 to 73 m at these stations. Regions of high S_V can be observed on the
385 MAD-Ridge seamount (seen as “white patches” at 150-250 m on the RGB composite image
386 between CTD stations 21 and 22), corresponding to aggregations of scatterers on the
387 seamount summit (Fig. 8).

388 3.4 Environmental factors influencing micronekton distribution during MAD-Ridge cruise

389 Median micronekton acoustic densities in the total water column and in the surface layer
390 were the highest within the cyclonic eddy compared to any other station categories ($p < 0.05$)
391 (Fig. 9a). The Flank/AC stations showed higher median micronekton acoustic densities of the
392 total water column compared to the Summit/AC stations (Fig. 9a). The Summit/AC stations
393 exhibited higher median micronekton acoustic densities in the surface layer compared to the
394 AC and Dipole I. stations ($p < 0.05$) (Fig. 9a). Micronekton acoustic densities in the deep

395 layer had the same overlapping ranges across all station categories except over the
396 Summit/AC stations ($p < 0.05$). Station 18, which was conducted at sunset (Table 1), within
397 the anticyclone showed high micronekton acoustic densities in the total water column (1461
398 $\pm 531 \text{ m}^2 \text{ nmi}^{-2}$), with the acoustic backscatter being distributed almost equally in the surface
399 and deep layers (506 ± 345 and $559 \pm 298 \text{ m}^2 \text{ nmi}^{-2}$ respectively) and in lower concentrations
400 in the intermediate layer ($397 \pm 154 \text{ m}^2 \text{ nmi}^{-2}$). This station can be considered as being
401 anomalous compared to the other anticyclonic stations. However, when this station was
402 removed from the above KW and pairwise analyses, the outcome remained unchanged.

403 To summarise, the cyclonic stations recorded the greatest micronekton acoustic densities of
404 the total water column and were characterised by negative SLA compared to the other station
405 categories (Fig. 9b). The cyclonic and shelf stations were characterised by the coldest
406 temperature at 100 m, shallower Fmax, the largest integrated chlorophyll *a* concentrations
407 between 2 and 200 m and the greatest mean zooplankton biovolumes (Fig. 9c-f). The
408 anticyclone recorded lower micronekton acoustic densities in the total water column
409 compared to the cyclonic ones (Fig. 9a). These stations were characterised by positive SLA,
410 warmer temperature values at 100 m, deeper Fmax, lower integrated chlorophyll *a* between 2
411 and 200 m and higher variability of zooplankton biovolumes compared to cyclonic stations
412 (Fig. 9b-f). The seamount summit stations did not exhibit remarkable micronekton acoustic
413 densities, nor integrated chlorophyll *a* and mean zooplankton biovolumes among station
414 categories (Fig. 9a, e, f). The station at the dipole interface recorded the lowest micronekton
415 acoustic densities, although values were not significant ($p < 0.05$) compared to the other
416 station categories, and were characterised by slightly negative SLA (Fig. 9a, b) and the
417 highest mean current speed of 99.1 m s^{-1} compared to all other stations (mean \pm S.D. of 40.6
418 $\pm 19.2 \text{ m s}^{-1}$).

419 3.5 Physical and biological oceanography at La Pérouse seamount

420 During the La Pérouse cruise, the seamount was under the influence of a weak cyclonic eddy
421 with geostrophic speeds of less than 1 m s^{-1} and satellite surface Absolute Dynamic
422 Topography heights of $\sim 1.1 \text{ m}$ (Fig. 10). ADCP measurements recorded a current velocity of
423 $\sim 10\text{-}40 \text{ cm s}^{-1}$ at the vicinity of La Pérouse seamount, in the upper 200 m (Marsac et al.,
424 2020). Surface temperatures ranged between 23 and 24°C , with a deeper thermocline (152-
425 181 m) at La Pérouse (flanks and offshore stations combined) compared to MAD-Ridge
426 cyclonic stations. Maximum chlorophyll a values of $0.18\text{-}0.44 \text{ mg m}^{-3}$ at Fmax depth between
427 65 and 140 m were recorded at all stations.

428 3.6 Comparison of micronekton acoustic densities at both seamounts

429 Wilcoxon tests performed for the 38 kHz frequency showed the overall acoustic densities of
430 the depth categories (surface, intermediate and deep) differed significantly between La
431 Pérouse and MAD-Ridge and between day and night ($p < 0.05$) along the transects mapped in
432 Fig. 11. The mean acoustic densities for the 38 kHz frequency of the total water column (10-
433 735 m) were lower over La Pérouse summit and flanks (Fig. 11a) both during the day ($653 \pm$
434 $689 \text{ m}^2 \text{ nmi}^{-2}$) and night ($903 \pm 600 \text{ m}^2 \text{ nmi}^{-2}$) compared to MAD-Ridge (Day: 1448 ± 1268
435 $\text{m}^2 \text{ nmi}^{-2}$; Night: $2261 \pm 1035 \text{ m}^2 \text{ nmi}^{-2}$) summit and flanks (Fig. 11b). During the day and
436 night, the surface layer gathered greater percentage acoustic responses compared to the deep
437 layer both at La Pérouse (Day, Surface: 87.5% ; Deep: 7.2% ; Night, Surface: 94.2% , Deep:
438 0.6%) and MAD-Ridge (Day, Surface: 57.2% ; Deep: 34.6% ; Night, Surface: 74.3% , Deep:
439 17.0%). The intermediate layer gathered percentage acoustic densities of 5 to 9% both during
440 the day and night and at both seamounts.

441 RGB composite images showed relatively low but dominant 38 kHz backscatter between
442 depths of ~ 20 and 60 m both at La Pérouse (Fig. 12a) and MAD-Ridge seamounts (Fig. 12b)
443 during the day. A stronger response to the 120 kHz frequency compared to the 38 kHz was
444 observed between ~ 100 and 180 m depths at La Pérouse and between ~ 100 to 125 m depths

445 at MAD-Ridge during the day. At night, the 38 kHz backscatter was stronger and more
446 dominant compared to the 70 kHz backscatter between depths of ~20 and 180 m both at La
447 Pérouse and MAD-Ridge (Fig. 12c and 12d). Regions of high acoustic densities (seen as
448 “white patches” on RGB composite images) were observed on La Pérouse and MAD-Ridge
449 summits both during the day and night (Fig. 12a, b, c and d).

450

451 **4. Discussion**

452 4.1 Oceanographic conditions during the MAD-Ridge and La Pérouse cruises

453 This study demonstrated the strong influence of mesoscale cyclonic and anticyclonic eddies
454 on the physical and biological properties at MAD-Ridge seamount. The doming of isotherms
455 and shallowing of the Fmax depth was observed within the cyclonic eddy during the MAD-
456 Ridge cruise. Such processes are associated with eddy-induced pumping and upwelling of
457 cool, nutrient-rich waters, triggering an increase in primary production in the photic layer
458 (McGillicuddy and Robinson, 1997; McGillicuddy et al., 1998; Klein and Lapeyre, 2009;
459 Huggett, 2014; Singh et al., 2015). Phytoplankton within mesoscale cyclonic eddies can also
460 grow in response to advection and subsequent retention of surrounding nutrient-rich waters
461 within eddies (José et al., 2014; Lamont et al., 2014). The anticyclonic eddy in this study was
462 characterised by a deeper thermocline and Fmax, with a decrease in productivity in the photic
463 layer than in the cyclonic eddy.

464 The Madagascar shelf also had a significant effect on the physical and biological processes
465 during the MAD-Ridge cruise. The thermocline and Fmax depth were shallower on the shelf
466 than at the other stations within the anticyclonic eddy. Previous studies have shown that the
467 coastal regions south of Madagascar are more productive than surrounding waters (Raj et al.,
468 2010; Pripp et al., 2014; Ramanantsoa et al., 2018; Annasawmy et al., 2019) owing to coastal
469 upwelling events driven by interactions between the East Madagascar Current and the

470 continental shelf and by upwelling favourable winds (Ramanantsoa et al., 2018). This
471 productivity can be entrained by mesoscale features that spin off the East Madagascar
472 Current, farther south, potentially towards MAD-Ridge (Noyon et al., 2018; Ockhuis et al.,
473 2017).

474 La Pérouse seamount, on the other hand, is located on the edge of the ISSG and was under
475 the influence of a weak mesoscale eddy field during the cruise there, reflecting average
476 conditions observed throughout the year in this region, as shown by Pous et al. (2014) using
477 the OSCAR product (https://podaac.jpl.nasa.gov/dataset/OSCAR_L4_OC_third-deg). Apart
478 from disturbances caused by the seamount to circulation, phytoplankton and zooplankton at a
479 small scale along the flanks (Marsac et al., 2020), the average conditions in the La Pérouse
480 area with relatively deep thermocline and Fmax depth, were typical of the oligotrophic ISSG
481 province. Overall, during the time of the cruises, sea surface chlorophyll concentrations were
482 twice as low within the region of the La Pérouse seamount as at the MAD-Ridge seamount
483 (Annasawmy et al., 2019).

484 4.2 Diel vertical migration of micronekton

485 Micronekton is a diverse group of organisms capable of demonstrating various swimming
486 behaviours (active swimming or passive drifting) and vertical migration strategies (diel
487 migrants, semi-migrants or non-migrants) (Brodeur and Yamamura 2005). In this study, the
488 different DVM patterns of micronekton were observed. Vertically migrating organisms
489 ascended to the surface (above 200 m) at sunset and descended below 400 m at sunrise in the
490 vicinity of both MAD-Ridge and La Pérouse, whereas only a small proportion of non-migrant
491 or semi-migrant micronekton remained in the deep layer by day at both seamounts. On
492 average, a difference of $595 \text{ m}^2 \text{ nmi}^{-2}$ to $1719 \text{ m}^2 \text{ nmi}^{-2}$ was recorded between day and night
493 periods at MAD-Ridge (West-East and South-North transects) and a difference of 790 m^2
494 nmi^{-2} between day and night at La Pérouse. These differences between alternate day and

495 night periods are likely caused either by the vertical migration of micronekton towards the
496 surface at night for feeding purposes, sometimes from layers deeper than 735 m (i.e. beyond
497 the range set for the 38 kHz transducer in this study), and/or the lateral advection of
498 organisms.

499 Micronekton acoustic densities were greater in the surface layer than in the deep layer during
500 the day at cyclonic eddy stations. This particular finding contradicts the general paradigm that
501 micronekton are located in deeper layers by day (eg. Baliño and Aksnes, 1993; Andersen et
502 al., 1998; Bertrand et al., 1999; Lebourges-Dhaussy et al., 2000; Benoit-Bird and Au, 2004;
503 Domokos et al., 2010; Godø et al., 2009, 2012; Drazen et al., 2011; Béhagle et al., 2014;
504 Menkes et al., 2015; Béhagle et al., 2017; Bianchi and Mislán, 2016; Annasawmy et al.,
505 2018). Micronekton do not only undertake direct swimming in vertical and horizontal planes,
506 but may also drift passively. Previous studies have reported passive drifting of the
507 mesopelagic myctophid *Benthosema glaciale* with swimming speeds of 0-0.02 m s⁻¹ along
508 weak tidal currents and short bouts of active swimming in a vertical direction with swimming
509 speeds of 0.05 m s⁻¹, possibly during feeding (Torgersen and Kaartvedt, 2001; Kaartvedt et
510 al., 2009). This species has also been reported to undertake reverse DVM, ascending to
511 approximately 200 m by day to forage on midwater plankton (Kaartvedt et al., 2009). The
512 reverse DVM pattern is not common, with only some species of zooplankton (Ohman et al.,
513 1983; Lampert, 1989) and mesopelagic fish having been reported to ascend to the surface
514 layer during the day to optimise feeding opportunities (Lebourges-Dhaussy et al., 2000;
515 Kaartvedt et al., 2009).

516 Some micronekton taxa may also preferentially stay in the surface layer during the day to
517 reduce competition during feeding. The micronekton species *Myctophum asperum*,
518 *Myctophum nitidulum*, *Symbolophorus evermanni*, and *Chromis brevirostis* showed delayed
519 vertical migration at night in the Kuroshio region of the western North Pacific, with specific

520 peak feeding hours and specialisation on different food organisms in order to reduce
521 competition (Watanabe et al., 2002). Daylight surface observations are rare but were made
522 for the mesopelagic fish *Benthoosema pterotum* in the Gulf of Oman (Gjørseter, 1978, 1984),
523 the myctophid *Benthoosema pterota* off the coast of Central America (Alverson, 1961) and the
524 myctophid *Vinciguerrria nimbaria* in the eastern Tropical Atlantic (Marchal and Lebourges-
525 Dhaussy, 1996; Lebourges-Dhaussy et al., 2000). The reasons for the daylight surface
526 occurrence of *V. nimbaria* has been linked to the presence of potential preys such as
527 zooplankton at the Fmax depth (Lebourges-Dhaussy et al., 2000). Previous studies have also
528 found the deep-dwelling cod *Micromesistius poutassou* which usually resides at a depth of
529 300-500 m, migrating to the surface of anticyclonic eddies probably to enhance feeding
530 opportunities (Godø et al., 2012). Micronekton organisms within the cyclonic eddy during
531 MAD-Ridge might have adopted a combination of these strategies and this possibility is
532 discussed in more detail below.

533 4.3 Influence of mesoscale features on micronekton vertical and horizontal distribution

534 As shown earlier, the vertical and horizontal distributions of micronekton at MAD-Ridge
535 were significantly influenced by mesoscale processes linked to the presence of cyclonic and
536 anticyclonic eddies. The daytime s_A values within the eddy dipole interface were the lowest
537 relative to the other hydrographic station categories used in this analysis. Harris et al. (2020)
538 also recorded lower larval fish densities at the eddy dipole interface than at cyclonic and
539 anticyclonic circulation stations. This can be attributed to the strong currents measured at this
540 location that have led to the dispersion of micronekton communities. Alternatively,
541 micronekton may have migrated below the depth range scanned by the 38 kHz transducer at
542 that station due to a combination of strong currents and daytime light intensities.

543 Overall, acoustic densities of the total water column recorded within the cyclonic eddy were
544 approximately twice as great as those recorded within the anticyclonic circulation during both

545 day and night. The integrated chlorophyll *a* and zooplankton biovolume maxima found in the
546 cyclonic eddy, matched the micronekton maxima, during day and night. Micronekton
547 biomass is reported to be dependent on the availability of planktonic prey (Menkes et al.,
548 2015), and hence on the oceanographic drivers of plankton production, as observed in this
549 study. In the anticyclonic eddy, the downwelling mechanism of nutrient-depleted surface
550 waters may have led to a reduction of chlorophyll *a* concentrations in the euphotic zone, and
551 a subsequent reduction in mesozooplankton abundance and micronekton acoustic densities
552 during both day and night. Previous studies conducted in the Mozambique Channel have also
553 reported lesser micronekton acoustic densities in anticyclonic relative to cyclonic eddies
554 (Béhagle et al., 2014). However, the same authors pointed out some variability in eddy-
555 induced biological responses, with one case of higher micronekton density in an anticyclonic
556 eddy that was attributed to larger and more mobile organisms that are less influenced by
557 mesoscale features than smaller organisms.

558 The RGB composite images have revealed the presence of a strong and dominant 38 kHz
559 backscatter in the surface layer during the day across the cyclonic eddy (Fig 3c). Previous
560 studies have demonstrated that epi- and mesopelagic fish with small gas-filled swimbladders
561 and gelatinous plankton with gas inclusions dominate the 38 kHz frequency (Porteiro and
562 Sutton, 2007; Kloser et al., 2002, 2009; Davison et al., 2015; Cascão et al., 2017; Proud et al.,
563 2018; Annasawmy et al., 2019). The occurrence of these organisms at the surface (10-200 m)
564 by day may be considered a response to the cyclonic eddy exhibiting relatively high
565 integrated chlorophyll *a* concentrations and zooplankton biovolumes. The question arises,
566 though, whether these micronekton species showed reverse migration strategies and actively
567 remained in the shallow layer by day or whether they were passively entrained with the
568 current within the cyclonic circulation. This shallow scattering layer may also have consisted
569 of gelatinous organisms, which as other zooplankton, responded to the localised cyclonic
570 productivity. The mesoscale cyclonic eddy may also have provided physical mechanisms that

571 led to zooplankton retention and concentration, thereby increasing the encounter rate between
572 micronekton and their prey. The micronekton organisms, likely epi- and mesopelagic fish,
573 would then preferentially stay in the surface layer by day to increase their feeding
574 opportunities.

575 4.4 Influence of seamounts on micronekton vertical and horizontal distributions

576 Dense aggregations of scatterers were observed over deep topographic features labelled X
577 and Y peaking at 430 m and 460 m, during night-time and sunrise, respectively (Figure 3b).
578 These dense aggregations may have been migrating during the time of the cruise, upwards
579 over feature X at night or downwards at feature Y at sunrise. Alternatively, they may be non-
580 migrating organisms that remained preferentially associated with these topographic features
581 during day and night. Studies have suggested that the bottom-trapping mechanism as well as
582 the horizontal flux of non-migrating zooplankton maintain the densities of zooplanktivorous
583 fish at seamounts of intermediate depth (Genin and Dower, 2007). A range of other factors
584 such as the quiescent shelters offered by these topographies and the absence of shallow
585 diving predators (Porteiro and Sutton, 2007) may also account for the presence of these dense
586 aggregations at the features labelled X and Y.

587 Micronekton acoustic densities over the summit and flanks of MAD-Ridge were lower than
588 the acoustic densities recorded within the cyclonic eddy and over the Madagascar shelf.
589 However, the acoustic densities surrounding MAD-Ridge's summit and flanks were greater
590 than those recorded in the vicinity of the summit and flanks of La Pérouse. Although there
591 were clear mechanisms leading to enhanced productivity within the cyclonic eddy and over
592 the Madagascar shelf, the local physical and biological dynamics over La Pérouse and MAD-
593 Ridge seamounts were less straightforward. No clear enhancement in micronekton acoustic
594 densities was observed over MAD-Ridge compared with the surrounding vicinity (within 14
595 nautical miles of the summit) at the time of the cruises (Annasawmy et al., 2019).

596 In the literature, Taylor columns that form over seamounts are often considered as physical
597 processes that are capable of enhancing productivity and isolating the seamount waters from
598 the large-scale environment (Genin and Boehlert, 1985; Dower et al., 1992; Genin, 2004).
599 The α , Ro and Bl values were above the threshold set in literature (Chapman and Haidvogel,
600 1992; White et al., 2007) at both La Pérouse and MAD-Ridge during the cruises. The
601 mesoscale eddy activity in the MAD-Ridge area may have dominated any potential seamount
602 effect. The summit of MAD-Ridge during most of the cruise was under the influence of the
603 anticyclonic eddy with current speeds exceeding 0.5 m s^{-1} , thus making the formation of a
604 Taylor column very unlikely. The MAD-Ridge's seamount shape may also not be favourable
605 to the formation of such features because the threshold set for α values in theoretical
606 calculations was exceeded. Additionally, because of the presence of the anticyclonic eddy
607 feature over MAD-Ridge's summit, there was a downward deflection of isotherms between
608 the surface and $\sim 200 \text{ m}$, instead of an uplifting as seen across other studies (Genin and
609 Boehlert 1985; Boehlert and Genin, 1987; Dower and Mackas, 1996). MAD-Ridge is located
610 in an "eddy corridor" to the south of Madagascar. Previous studies have found evidence of a
611 westward drift of eddies at an estimated speed of $7.3 \pm 1.7 \text{ cm s}^{-1}$ in the vicinity of the
612 pinnacle, along 27°S and 45°E (Pollard and Read., 2017). Phytoplankton entrapment during
613 several weeks would be needed to allow growth of zooplankton and to attract micronekton
614 species (Genin and Boehlert 1985; Boehlert and Genin, 1987; Dower et al., 1992). In such a
615 dynamic system, strong currents may continuously sweep away phytoplankton cells from the
616 summit. Phytoplankton retention mechanisms may not be sufficiently long to have a
617 significant impact on higher trophic levels such as zooplankton and micronekton, potentially
618 explaining the lower micronekton acoustic densities recorded directly above MAD-Ridge's
619 summit during the cruise relative to the cyclonic eddy and shelf stations.

620 La Pérouse's pinnacle is believed to cause disruptions in the current velocities because flank
621 stations (within 3 km of the summit) exhibited a larger diversity of current velocities and

622 directions than control stations (10-21 km away) (Marsac et al., 2020). Over La Pérouse
623 seamount, the formation of a Taylor column was also very unlikely to have occurred because
624 current speeds of 0.3 m s^{-1} and greater were recorded. The complex crescent shape of the
625 seamount may not be favourable for the development of a steady anticyclonic circulation.
626 The La Pérouse wider region is under the influence of the anticyclonic circulation pattern of
627 the ISSG province characterised by a deep thermocline, a halocline and a DCM at 100-150
628 m, with chlorophyll *a* concentrations $<0.3 \text{ mg m}^{-3}$ between the surface and 200 m as observed
629 in our study and in Jena et al. (2012, 2013). Overall mean acoustic densities of micronekton
630 at the La Pérouse seamount were thus typical of those of the ISSG province both during day
631 and night (Annasawmy et al., 2018).

632 Common to both La Pérouse and MAD-Ridge seamounts is the presence of dense
633 aggregations of scatterers (seen as “white patches” on RGB composite images, Fig. 8 and
634 12a-d) directly above the summits during day and night. A combination of trawls and
635 acoustic data revealed these dense aggregations to consist of the myctophids *Diaphus*
636 *suborbitatis* (both La Pérouse and MAD-Ridge), *Benthoosema fibulatum*, *Hygophum hygomii*
637 and the benthopelagic fish *Cookeolus japonicus* on MAD-Ridge’s summit and flanks
638 (Annasawmy et al., 2019). Populations of *D. suborbitalis* have also been reported to be
639 located between 500 and 600 m during the day along the flanks of the Equator seamount in
640 the Indian Ocean, and to ascend to the surface of the seamount at dusk to feed on copepods
641 (Gorelova and Prut’ko, 1985; Parin and Prut’ko, 1985; Porteiro and Sutton, 2007), while *B.*
642 *fibulatum* has been found associated with the Hawaiian Cross seamount in the Pacific (De
643 Forest and Drazen, 2009). Dense aggregations of scatterers were also observed above a ridge
644 off the coast of Baja California and was thought to consist of the fish *Sebastes*, anchovy
645 and juvenile hake that prey on migrating zooplankton (Isaacs and Schwartzlose, 1965).
646 Similar aggregations of scatterers were observed on the South East Hancock seamount in the
647 central North Pacific, consisting of resident populations of the fish *Maurolicus muelleri* and

648 the mysid *Gnathopausia longispina* (Boehlert et al., 1994). Time-series of acoustic transects
649 showed these organisms to be concentrated on the seamount flanks at 400 m, before rising to
650 the surface at dusk and streaming vertically downwards at dawn, with some scatterers
651 remaining above the flanks at 170 m even during daylight. The association of these fish with
652 seamounts may confer some selective advantages such as enhanced feeding opportunities,
653 increased habitat diversity (Wilson and Boehlert, 2004; Porteiro and Sutton, 2007), shelter
654 areas for spawning, or decreased energy loss by using the seamount as a shelter during non-
655 feeding intervals (Cascão et al., 2017).

656 The maintenance of a population at a seamount also depends on local recruitment or
657 advection of eggs and larvae from the shelf or neighbouring islands and seamounts (Boehlert
658 et al., 1994; Diekmann et al., 2006). According to Harris et al. (2020), higher larval densities
659 mostly of the families Myctophidae, Bregmacerotidae, Gonostomatidae and Molidae were
660 recorded at MAD-Ridge's summit. According to those authors, this observation points to
661 some local spawning processes at the pinnacle. The MAD-Ridge seamount is close to shallow
662 and deep topographic structures and to the Madagascar shelf, features from which larvae
663 might have been advected (Crochelet et al., 2020). The presence of a greater proportion of
664 neritic species over the summit of MAD-Ridge seamount relative to La Pérouse seems to
665 favour this hypothesis (Harris et al., 2020). The mesoscale activity on the Madagascar shelf
666 and at MAD-Ridge may allow the periodic replenishment of advected larvae over the
667 pinnacle (Harris et al., 2020; Crochelet et al., 2020), corresponding with enhanced
668 micronekton acoustic densities compared to La Pérouse.

669

670 **5. Concluding Remarks**

671 This study has suggested a link between the physical processes leading to enhanced
672 productivity and the biological response of micronekton. Two main processes were identified

673 to have a positive effect on the observed productivity: 1) the influence of the cyclonic eddy
674 through the enrichment of surface waters, 2) the advection of shelf waters with high
675 chlorophyll *a* concentrations. La Pérouse and MAD-Ridge seamounts did not show any
676 enhanced biomass of micronekton, as reported to be the case for other seamounts. However,
677 despite the differing productivity levels at both seamounts, dense aggregations of scatterers
678 were observed on the summits during day and night. This study has therefore suggested that
679 seamount-associated species were the only seamount effect detected and that in a highly
680 dynamic environment like south of Madagascar, mesoscale features have a stronger influence
681 than seamounts on micronekton acoustic densities.

682

683

684 **Acknowledgements**

685 We acknowledge the work carried out by the non-scientific and scientific staff on board the
686 RV *Antea* in taking part in the data acquisition and data processing. The study was mainly
687 supported by the Flotte Océanographique Française (French Oceanographic Fleet) and IRD in
688 relation to the logistics of the RV *Antea*. Additional funding was also received from Région
689 Reunion (Réunion Regional Council) for the La Pérouse cruise, and from the Fonds Français
690 pour l'Environnement Mondial (FFEM) as part of the FFEM-SWIO project on Areas Beyond
691 National Jurisdiction (ABNJ) of the South West Indian Ocean for the MAD-Ridge cruise.
692 The first author was the beneficiary of a doctoral bursary granted by the Institut de Recherche
693 pour le Développement (IRD, France) and the ICEMASA French-South African International
694 Laboratory.

References

- Alverson, F.G., 1961. Daylight Surface Occurrence of Myctophid Fishes Off the Coast of Central America. *Pac Sci.* 15(3): 483. <http://hdl.handle.net/10125/9088>
- Andersen, V., François, F., Sardou, J., Picheral, M., Scotto, M., Nival, P., 1998. Vertical distributions of macroplankton and micronekton in the Ligurian and Tyrrhenian Seas (northwestern Mediterranean). *Oceanologica Acta.* 21(5): 655-676.
- Annasawmy, P., Ternon, J.F., Marsac, F., Cherel, Y., Béhagle, N., Roudaut, G., Lebourges-Dhaussy, A., Demarcq, H., Moloney, C.L., Jaquemet, S., Ménard, F., 2018. Micronekton diel migration, community composition and trophic position within two biogeochemical provinces of the South West Indian Ocean: Insight from acoustics and stable isotopes. *Deep-Sea Res. I.* 138: 85-97. <https://doi.org/10.1016/j.dsr.2018.07.002>
- Annasawmy, P., Ternon, J-F., Cotel, P., Demarcq, H., Cherel, Y, Romanov, E., Roudaut, G., Lebourges-Dhaussy, A., Ménard, F., Marsac, F. 2019. Micronekton distribution and assemblages at two shallow seamounts in the south-western Indian Ocean: Insights from acoustics and mesopelagic trawl data. *Prog. Oceanogr.* <https://doi.org/10.1016/j.pocean.2019.102161>
- Bakun, A., 2006. Fronts and eddies as key structures in the habitat of marine fish larvae: opportunity, adaptive response and competitive advantage. *Sci. Mar.* 70, 105–122. <https://doi.org/10.3989/scimar.2006.70s2105>
- Baliño, B.M, Aksnes, D.L., 1993. Winter distribution and migration of the sound scattering layers, zooplankton and micronekton in Masfjorden, western Norway. *Mar. Ecol. Prog. Ser.* 102: 35-50. <https://www.int-res.com/articles/meps/102/m102p035.pdf>
- Béhagle, N., du Buisson, L., Josse, E., Lebourges-Dhaussy, A., Roudaut, G., Ménard, F., 2014. Mesoscale features and micronekton in the Mozambique Channel: An acoustic approach. *Deep-Sea Res. II.* 100: 164-173. <http://dx.doi.org/10.1016/j.dsr2.2013.10.024>
- Béhagle, N., Cotté, C., Lebourges-Dhaussy, A., Roudaut, G., Duhamel, G., Brehmer, P., Josse, E., Cherel, Y., 2017. Acoustic distribution of discriminated micronektonic organisms from a bi-frequency processing: The case study of eastern Kerguelen oceanic waters. *Progress in Oceanography*, 156: 276-289. <https://doi.org/10.1016/j.pocean.2017.06.004>
- Benitez-Nelson, C.R., McGillicuddy, D. J., 2008. Mesoscale Physical-Biological-Biogeochemical Linkages in the Open Ocean: An Introduction to the results of the E-Flux and EDDIES Programs. *Deep-Sea Res. II.* 55(10-13): 1133–38. <https://doi.org/10.1016/j.dsr2.2008.03.001>
- Benoit-Bird, K.J., Au, W.W.L, 2004. Diel migration dynamics of an island-associated sound-scattering layer. *Deep-Sea Res. I.* 51: 707-719. doi:10.1016/j.dsr.2004.01.004
- Bertrand, A., Le Borgne, R., Josse, E., 1999. Acoustic characterisation of micronekton distribution in French Polynesia. *Mar. Ecol. Prog. Ser.* 191: 127-140. doi:10.3354/meps191127
- Bertrand, A., Bard, F.X. Josse, E., 2002. Tuna food habits related to the micronekton distribution in French Polynesia. *Mar Biol.* 140: 1023-1037. doi:10.1007/s00227-001-0776-3
- Bianchi, D., Stock, C., Galbraith, E.D., Sarmiento, J.L., 2013. Diel vertical migration: Ecological controls and impacts on the biological pump in a one-dimensional ocean model. *Global Biogeochem. Cycles.* 27: 478-491. doi:10.1002/gbc.20031.
- Bianchi, D., Mislán, K.A.S., 2016. Global patterns of diel vertical migration times and velocities from acoustic data. *Limnol. Oceanogr.* 61: 353-364. doi: 10.1002/lno.10219

- Boehlert, G.W., Genin, A., 1987. A review of the effects of seamounts on biological processes. B. Keating, P. Fryer, R. Batiza (Eds.), Seamounts, islands and atolls, American Geophysical Union, Washington, D.C (1987), pp. 319-334
- Boehlert, G.W., 1988. Current-Topography Interactions at Mid-Ocean Seamounts and the Impact on Pelagic Ecosystems. *GeoJournal*, 16.1: 45-52.
- Boehlert, G.W., Wilson, C.D., Mizuno, K., 1994. Populations of the Sternoptychid Fish *Maurolicus muelleri* on Seamounts in the Central North Pacific. *Pac. Sci.* 48(1): 57-69.
- Brierley, A.S., 2014. Diel vertical migration. *Current Biology*. 24(22): R1074-R1076. <https://doi.org/10.1016/j.cub.2014.08.054>
- Brodeur, R.D., Seki, M.P., Pakhomov, E.A., Suntsov, A.V., 2005. Micronekton-What are they and why are they important? *PICES Press* 14: 7–11.
- Brodeur, R.D., Yamamura, O., 2005. *PICES Scientific Report No. 30 Micronekton of the North Pacific*. *PICES Scientific Report*, Sidney, B.C., Canada, pp. 1–115.
- Cascão, I., Domokos, R., Lammers, M.O., Marques, V., Domínguez, R., Santos, R.S., Silva, M.A., 2017. Persistent Enhancement of Micronekton Backscatter at the Summits of Seamounts in the Azores. *Front. Mar. Sci.* 4: 25. <https://doi.org/10.3389/fmars.2017.00025>
- Catul, V., Gauns, M., Karuppasamy, P.K., 2011. A review of mesopelagic fishes belonging to family Myctophidae. *Rev. Fish Biol. Fisheries*. 21: 339-354. doi: 10.1007/s11160-010-9176-4
- Chapman, D.C., Haidvogel, D.B., 1992. Formation of Taylor Caps over a tall isolated seamount in a stratified ocean. *Geophysical and Astrophysical Fluid Dynamics*. 64: 31–65.
- Chelton, D.B., Schlax, M.G., Samelson, R.M., 2011. Global observations of nonlinear mesoscale eddies. *Prog. Oceanogr.* 91: 167-216. <https://doi.org/10.1016/j.pocean.2011.01.002>
- Cherel, Y., Fontaine, C., Richard, P., Labat, J-P., 2010. Isotopic niches and trophic levels of myctophid fishes and their predators in the Southern Ocean. *Limnol. Oceanogr.* 55(1): 324-332. <https://doi.org/10.4319/lo.2010.55.1.0324>
- Cherel, Y., Romanov, E.V., Annasawmy, P., Thibault, D., Ménard, F., 2020. Micronektonic fish species over three seamounts in the southwestern Indian Ocean and myctophid infestation by the copepod *Cardiodectes bellotti*. *Deep-Sea Res. II*.
- Crochelet, E., Barrier, N., Andrello, M., Marsac, F., Spadone, A., Lett, C., 2020. Connectivity between seamounts and coastal ecosystems in the South West Indian Ocean. *Deep Sea Res. Part II*.
- Danckwerts, D.K., McQuaid, C.D., McGregor, G.K., Dwight, R., Le Corre, M., Jaquemet, S., 2014. Biomass consumption by breeding seabirds in the western Indian Ocean: indirect interactions with fisheries and implications for management. *ICES J. Mar. Sci.* 71(9): 2589-2598. doi:10.1093/icesjms/fsu093
- Davison, P.C., Koslow, J.A., Kloser, R.J. 2015. Acoustic biomass estimation of mesopelagic fish: backscattering from individuals, populations, and communities. *ICES J. Mar. Sci.* 72(5): 1413-1424. doi:10.1093/icesjms/fsv023
- De Forest, L., Drazen, J., 2009. The influence of a Hawaiian seamount on mesopelagic micronekton. *Deep-Sea Res I*. 56: 232-250. doi:10.1016/j.dsr.2008.09.007
- De Robertis, A., Higginbottom, I., 2007. A post-processing technique to estimate the signal-to-noise ratio and remove echosounder background noise. *ICES J. Mar. Sci.* 64: 1282-1291. <https://doi.org/10.1093/icesjms/fsm112>
- Diekmann, R., Nellen, W., Piatkowski, U., 2006. A multivariate analysis of larval fish and paralarval cephalopod assemblages at Great Meteor Seamount. *Deep-Sea Res. I*. 53: 1635-1657. doi:10.1016/j.dsr.2006.08.008

- Domokos, R., Pakhomov, E.A., Suntsov, A.V., Seki, M.P., Polovina, J.J., 2010. Acoustic Characterization of the Mesopelagic Community off the Leeward Coast of Oahu Island, Hawaii. In: Report of the Advisory Panel on Micronekton Sampling Inter-calibration Experiment Edition: 38 Publisher: PICES Scientific Report [Eds]: Pakhomov, E.A., Yamamura, O.
- Dower, J., Freeland, H., Juniper, K., 1992. A strong biological response to oceanic flow past Cobb Seamount. *Deep-Sea Res.* 39(7/8): 1139–1145. [https://doi.org/10.1016/0198-0149\(92\)90061-W](https://doi.org/10.1016/0198-0149(92)90061-W)
- Dower, J.F., Mackas, D.L., 1996. “Seamount effects” in the zooplankton community near Cobb Seamount. *Deep-Sea Res. I.* 43(6): 837–858. [https://doi.org/10.1016/0967-0637\(96\)00040-4](https://doi.org/10.1016/0967-0637(96)00040-4)
- Drazen, J.C., De Forest, L.G., Domokos, R., 2011. Micronekton abundance and biomass in Hawaiian waters as influenced by seamounts, eddies and the moon. *Deep-Sea Res. I.* 58: 557-566. doi:10.1016/j.dsr.2011.03.002
- Dufois, F., Hardman-Mountford, N.J., Greenwood, J., Richardson, A.J., Feng, M., Herbette, S., Matear, R., 2014. Impact of eddies on surface chlorophyll in the South Indian Ocean. *J. Geophys. Res. Oceans.* 119: 8061–8077. <https://doi.org/10.1002/2014JC010164>
- Foote, K.G., Knudsen, H.P., Vestnes, G., MacLennan, D.N., Simmonds, E.J., 1987. Calibration of acoustic instruments for fish density estimation: a practical guide. *ICES Coop. Res. Rep.* 144: 1-69.
- Genin, A., Boehlert, G.W., 1985. Dynamics of temperature and chlorophyll structures above a seamount: An oceanic experiment. *J. Mar. Res.* 43: 907-924.
- Genin, A., 2004. Bio-physical coupling in the formation of zooplankton and fish aggregations over abrupt topographies. *J. Mar. Sci.* 50: 3-20. doi:10.1016/j.jmarsys.2003.10.008
- Genin, A., Dower, J.F., 2007. Seamount Plankton Dynamics. In: Pitcher, T.J., Morato, T., Hart, P.J.B., Clark, M.R., Haggan, N., Santos, R.S. (Eds), *Seamounts: Ecology, Fisheries & Conservation*. Blackwell Publishing Ltd, Oxford, UK, pp. 85-100.
- Gjøsaeter, J., 1978. Aspects of the distribution and ecology of the Myctophidae from the Western and Northern Arabian Sea. *Development Report Indian Ocean Programme*, 43: 62–108.
- Gjøsaeter, J., 1984. Mesopelagic fish, a large potential resource in the Arabian Sea. *Deep-Sea Res. Part A.* 31:1019–1035.
- Godø, O.R., Patel, R., Pedersen, G., 2009. Diel migration and swimbladder resonance of small fish: some implications for analyses of multifrequency echo data. *ICES J. Mar. Sci.* 66: 1143–1148. <https://doi.org/10.1093/icesjms/fsp098>
- Godø, O.R., Samuelson, A., Macaulay, G.J., Patel, R., Hjøllø, S.S., Horne, J., Kaartvedt, S., Johannessen, J.A., 2012. Mesoscale Eddies Are Oases for Higher Trophic Marine Life. *PLoS ONE.* 7(1): e30161. <https://doi.org/10.1371/journal.pone.0030161>
- Gorelova T.A., Prutko, V.G., 1985. On feeding of *Diaphus suborbitalis* (Myctophidae, Pisces) in the equatorial Indian Ocean. *Okeanologiya.* 25: 677-684 (in Russian).
- Gorsky, G., Ohman, M.D., Picheral, M., Gasparini, S., Stemmann, L., Romagnan, J-B., Gawood, A., Pesant, S., García-Lomas, C., Prejger, F., 2010. Digital zooplankton image analysis using the ZooScan integrated system. *J. Plankton Res.* 32(3): 285-303. doi:10.1093/plankt/fbp124
- Guinet, C., Cherel, Y., Ridoux, V., Jouventin, P., 1996. Consumption of marine resources by seabirds and seals in Crozet and Kerguelen waters: changes in relation to consumer biomass 1962-85. *Antarctic Science.* 8(1): 23-30.
- Halo, I., Backeberg, B., Penven, P., Ansoerge, I., Reason, C., Ullgren, J.E., 2014. Eddy properties in the Mozambique Channel: A comparison between observations and two

- numerical ocean circulation models. *Deep-Sea Res. II.* 100: 38-53. <http://dx.doi.org/10.1016/j.dsr2.2013.10.015>
- Harris, S.A., Noyon, M., Roberts, M., Marsac, F., 2020. Ichthyoplankton assemblages at three shallow seamounts in the South West Indian Ocean: La Pérouse, MAD-Ridge and Walters Shoal. *Deep Sea Res. Part II.*
- Heywood, K.J., 1996. Diel vertical migration of zooplankton in the Northeast Atlantic. *Journal of Plankton Research.* 18(2): 163-184.
- Hidaka, K., Kawaguchi, K., Murakami, M., Takahashi, M., 2001. Downward transport of organic carbon by diel migratory micronekton in the western equatorial Pacific: its quantitative and qualitative importance. *Deep-Sea Res. I.* 48: 1923-1939.
- Huggett, J.A., 2014. Mesoscale distribution and community composition of zooplankton in the Mozambique Channel. *Deep-Sea Res. II.* 100: 119-135. <http://dx.doi.org/10.1016/j.dsr2.2013.10.021>
- Isaacs, J.D., Schwartzlose, R.A., 1965. Migrant Sound Scatterers: Interaction with the Sea Floor. *Science.* 150, 1810–1813. <https://doi.org/10.1126/science.150.3705.1810>
- Isern-Fontanet, J., Font, J., García-Ladona, E., Emelianov, M., Millot, C., Taupier-Letage, I., 2004. Spatial structure of anticyclonic eddies in the Algerian basin (Mediterranean Sea) analyzed using the Okubo-Weiss parameter. *Deep-Sea Res. II.* 51: 3009-3028. doi:10.1016/j.dsr2.2004.09.013
- Jaquemet, S., Ternon, J.F., Kaehler, S., Thiebot, J.B., Dyer, B., Bemanaja, E., Marteau, C., Le Corre, M., 2014. Contrasted structuring effects of mesoscale features on the seabird community in the Mozambique Channel. *Deep-Sea Res. II.* 100: 200-211. <http://dx.doi.org/10.1016/j.dsr2.2013.10.027>
- Jena, B., Swain, D., Avinash, K., 2012. Investigation of the biophysical processes over the oligotrophic waters of South Indian Ocean subtropical gyre, triggered by cyclone Edzani. *International Journal of Applied Earth Observation and Geoinformation* 18: 49-56. doi:10.1016/j.jag.2012.01.006
- Jena, B., Sahu, S., Avinash, K., Swain, D., 2013. Observation of oligotrophic gyre variability in the south Indian Ocean: Environmental forcing and biological response. *Deep-Sea Res. I.* 80: 1-10. <http://dx.doi.org/10.1016/j.dsr.2013.06.002>
- Johnston, D. W., McDonald, M., Polovina, J., Domokos, R., Wiggins, S., Hildebrand, J., 2008. Temporal patterns in the acoustic signals of beaked whales at Cross Seamount. *Biol. Lett.* 4: 208–211. <https://doi.org/10.1098/rsbl.2007.0614>
- José, Y.S., Aumont, O., Machu, E., Penven, P., Moloney, C.L., Maury, O., 2014. Influence of mesoscale eddies biological production in the Mozambique Channel: Several contrasted examples from a coupled ocean-biogeochemistry model. *Deep-Sea Res. II.* 100: 79-93. <http://dx.doi.org/10.1016/j.dsr2.2013.10.018>
- Judkins, D.C., Haedrich, R.L., 2018. The deep scattering layer micronektonic fish faunas of the Atlantic mesopelagic ecoregions with comparison of the corresponding decapod shrimp faunas. *Deep-Sea Res. I.* 136: 1-30. <https://doi.org/10.1016/j.dsr.2018.04.008>
- Kaartvedt, S., Røstad, A., Klevjer, T., Staby, A., 2009. Use of bottom-mounted echo sounders in exploring behavior of mesopelagic fishes. *Mar. Ecol. Prog. Ser.* 395, 109–118. <https://doi.org/10.3354/meps08174>
- Klein, P., Lapeyre, G., 2009. The Oceanic Vertical Pump Induced by Mesoscale and Submesoscale Turbulence. *Annu. Rev. Mar. Sci.* 1, 351–375. <https://doi.org/10.1146/annurev.marine.010908.163704>
- Kloser, R.J., Ryan, T., Sakov, P., Williams, A., Koslow, J.A., 2002. Species identification in deep water using multiple acoustic frequencies. *Canadian Journal of Fisheries and Aquatic Sciences.* 59:1065-1077.

- Kloser, R.J., Ryan, T.E., Young, J.W., Lewis, M.E., 2009. Acoustic observations of micronekton fish on the scale of an ocean basin: potential and challenges. *ICES J. Mar. Sci.* 66(6): 998–1006, <https://doi.org/10.1093/icesjms/fsp077>
- Kloser, R.J., Ryan, T.E., Keith, G., Gershwin, L., 2016. Deep-scattering layer, gas-bladder density, and size estimates using a two-frequency acoustic and optical probe. *ICES J. Mar. Sci.* 73(8): 2037-2048. DOI:10.1093/icesjms/fsv257
- Lamont, T., Barlow, R.G., Morris, T., van den Berg, M.A., 2014. Characterisation of mesoscale features and phytoplankton variability in the Mozambique Channel. *Deep Sea Res. Part II Top. Stud. Oceanogr.* 100: 94–105. <https://doi.org/10.1016/j.dsr2.2013.10.019>
- Lampert, W., 1989. The Adaptive Significance of Diel Vertical Migration of Zooplankton. *Functional Ecology*, 3(1): 21-27. doi:10.2307/2389671
- Lebourges-Dhaussy, A., Marchal, E., Menkès, C., Champalbert, G., Biessy, B., 2000. *Vinciguerria nimbaria* (micronekton), environment and tuna: their relationships in the Eastern Tropical Atlantic. *Oceanologica Acta.* 23(4): 515-528.
- Lehodey, P., Murtugudde, R., Senina, I., 2010. Bridging the gap from ocean models to population dynamics of large marine predators: A model of mid-trophic functional groups. *Prog. Oceanogr.* 84: 69-84. DOI:10.1016/j.pocean.2009.09.008
- Lévy, M., Klein, P., Treguier, A-M., 2001. Impact of sub-mesoscale physics on production and subduction of phytoplankton in an oligotrophic regime. *J. Mar. Res.* 59: 535-565.
- Lévy, M., Franks, P.J.S., Smith, K.F. 2018. The role of submesoscale currents in structuring marine ecosystems. *Nature Communications.* 9(4758). DOI: 10.1038/s41467-018-07059-3
- Longhurst, A., 2007. The Indian Ocean-Indian South Subtropical Gyre Province (ISSG). In: Academic Press (Ed.), *Ecological Geography of the Sea*, 2nd ed. Elsevier, USA, pp. 285.
- MacLennan, D.V., Fernandes, P.G., Dalen, J. 2002. A consistent approach to definitions and symbols in fisheries acoustics. *ICES J. Mar. Sci.* 59: 365-369. doi:10.1006/jmsc.2001.1158
- Mann, K.H., Lazier, J.R., 2006. *Dynamics of marine ecosystems: biological-physical interactions in the oceans.* (Third edition), John Wiley and Sons (2006).
- Marchal, E., Lebourges-Dhaussy, A., 1996. Acoustic evidence for unusual diel behaviour of a mesopelagic fish (*Vinciguerria nimbaria*) exploited by tuna. *ICES J. Mar. Sci.* 53, 443–447. <https://doi.org/10.1006/jmsc.1996.0062>
- Marsac, F., Annasawmy, P., Noyon, M., Demarcq, H., Soria, M., Rabearisoa, N., Bach, P., Cherel, Y., Grelet, J., Romanov, E., 2020. Seamount effect on circulation and distribution of ocean taxa at and near La Pérouse, a shallow seamount in the southwestern Indian Ocean. *Deep-Sea Res. Part II.*
- McGillicuddy, D.J., Robinson, A.R., 1997. Eddy-induced nutrient supply and new production in Sargasso Sea. *Deep-Sea Res. I.* 44(8): 1427-1450.
- McGillicuddy, D.J., Robinson, A.R., Siegel, D.A., Jannasch, H.W., Johnson, R., Dickey, T.D., McNell, J., Michaels, A.F., Knap, A.H., 1998. Influence of mesoscale eddies on new production in the Sargasso Sea. *Nature.* 394: 263–266.
- McGillicuddy, D.J., 2016. Mechanisms of Physical-Biological-Biogeochemical Interaction at the Oceanic Mesoscale. *Annu. Rev. Mar. Sci.* 8: 125-59. doi: 10.1146/annurev-marine-010814-015606
- Ménard, F., Benivary, H.D., Bodin, N., Coffineau, N., Le Loc'h, F., Mison, T., Richard, P., Potier, M., 2014. Stable isotope patterns in micronekton from the Mozambique Channel. *Deep-Sea Res II.* 100: 153-163. <https://doi.org/10.1016/j.dsr2.2013.10.023>
- Menkes, C.E., Allain, V., Rodier, M., Gallois, F., Lebourges-Dhaussy, A., Hunt, B.P.V., Smeti, H., Pagano, M., Josse, E., Daroux, A., Lehodey, P., Senina, I., Kestenare, E.,

- Lorrain, A., Nicol, S., 2015. Seasonal oceanography from physics to micronekton in the south-west Pacific. *Deep-Sea Res. II.* 113: 125-144. <http://dx.doi.org/10.1016/j.dsr2.2014.10.026>
- Mohn, C., Beckmann, A., 2002. The upper ocean circulation at Great Meteor Seamount. *Ocean Dyn.* 52: 179–193. <https://doi.org/10.1007/s10236-002-0017-4>
- Nishino, S., Itoh, M., Kawaguchi, Y., Kikuchi, T., Aoyama, M., 2011. Impact of an unusually large warm-core eddy on distributions of nutrients and phytoplankton in the southwestern Canada Basin during late summer/early fall 2010. *Geophysical Research Letters.* 38: L16602. doi:10.1029/2011GL047885, 2011
- Noyon, M., Morris, T., Walker, D., Huggett, J., 2018. Plankton distribution within a young cyclonic eddy off south-western Madagascar. *Deep Sea Res. II.* In Press. <https://doi.org/10.1016/j.dsr2.2018.11.001>
- Noyon, M., Rasoloarijao, Z., Huggett, J., Ternon, J-F., Roberts, M., 2020. Comparison of mesozooplankton communities at three shallow seamounts in the South West Indian Ocean. *Deep Sea Res. Part II.* <https://doi.org/10.1016/j.dsr2.2020.104759>
- Ockhuis, S., Huggett, J. A., Gouws, G., Sparks, C., 2017. The ‘suitcase hypothesis’: Can entrainment of meroplankton by eddies provide a pathway for gene flow between Madagascar and KwaZulu-Natal, South Africa?. *African J Mar. Sci.* 39(4): 435-451. <https://doi.org/10.2989/1814232X.2017.1399292>
- Ohman, M.D., Frost, B.W., Cohen, E.B., 1983. Reverse Diel Vertical Migration: An Escape from Invertebrate Predators. *Science.* 220(4604): 1404-1407. DOI: 10.1126/science.220.4604.1404
- Okubo, A., 1970. Horizontal dispersion of floatable particles in the vicinity of velocity singularities such as convergences. *Deep Sea Res.* 17: 445–454.
- Owen, R.W., 1980. Eddies of the California Current System: Physical and ecological characteristics, in *The California Islands: Proceedings of a Multidisciplinary Symposium*, edited by D. Power, 237 – 263. Santa Barbara Mus. of Nat. Hist., Santa Barbara, California.
- Owen, R.W., 1981. Fronts and eddies in the sea: mechanisms, interactions, and biological effects. 197-233 in Longhurst, A. R., [Ed]. *Analysis of marine ecosystems.* Academic Press, New York.
- Parin, N.V., Prutko, V.G., 1985. Thalassal mesobenthopelagic ichthyocoen over the Equator submarine rise in the western tropical Indian Ocean. *Okeanologia* 25: 1017-1020 (in Russian).
- Perrot Y., Brehmer P., Habasque J., Roudaut G., Béhagle N., Sarre A., Lebourges-Dhaussy A., 2018. Matecho: an open-source tool for processing fisheries acoustics data. *Acoustics Australia.* 46(2): 241-248. ISSN 1839-2571
- Pollard, R., Read, J., 2017. Circulation, stratification and seamounts in the Southwest Indian Ocean. *Deep-Sea Res. II.* 136: 36-43. <https://doi.org/10.1016/j.dsr2.2015.02.018>
- Porteiro, F.M., Sutton, T., 2007. Midwater Fish Assemblages and Seamounts, in: Pitcher, T.J., Morato, T., Hart, P.J.B., Clark, M.R., Haggan, N., Santos, R.S. (Eds.), *Seamounts: Ecology, Fisheries & Conservation.* Blackwell Publishing Ltd, Oxford, UK, pp. 101–116. <https://doi.org/10.1002/9780470691953.ch6>
- Potier, M., Marsac, F., Cherel, Y., Lucas, V., Sabatié, R., Maury, O., Ménard, F., 2007. Forage fauna in the diet of three large pelagic fishes (lancetfish, swordfish and yellowfin tuna) in the western equatorial Indian Ocean. *Fisheries Res.* 83: 60-72. doi:10.1016/j.fishres.2006.08.020
- Pous, S., Lazure, P., André, G., Dumas, F., Halo, I., Penven, P., 2014. Circulation around La Réunion and Mauritius islands in the south-western Indian Ocean: A modeling perspective. *J. Geophys. Res. Oceans.* 119: 1957-1976. doi:10.1002/2013JC009704

- Prupp, T., Gammelsrød, T., Krakstad, J.O., 2014. Physical influence on biological production along the western shelf of Madagascar. *Deep-Sea Res. II.* 100: 174-183. <http://dx.doi.org/10.1016/j.dsr2.2013.10.025>
- Proud, R., Handegard, N.O., Kloser, R.J., Cox, M.L., Brierley, A.S., 2018. From siphonophores to deep scattering layers: uncertainty ranges for the estimation of global mesopelagic fish biomass. *ICES J. Mar. Sci.* fsy037, <https://doi.org/10.1093/icesjms/fsy037>
- Raj, R.P., Peter, B.N., Pushpadas, D., 2010. Oceanic and atmospheric influences on the variability of phytoplankton bloom in the Southwestern Indian Ocean. *J. Mar. Syst.* 82, 217–229. <https://doi.org/10.1016/j.jmarsys.2010.05.009>
- Ramanantsoa, J.D., Krug, M., Penven, P., Rouault, M., Gula, J., 2018. Coastal upwelling south of Madagascar: Temporal and spatial variability. *J. Mar. Sci.* 178: 29-37. <http://dx.doi.org/10.1016/j.jmarsys.2017.10.005>
- Royer, T.C., 1978. Ocean Eddies Generated by Seamounts in the North Pacific. *Science* 199, 1063–1064. <https://doi.org/10.1126/science.199.4333.1063-a>
- Ryan, T.E., Downie, R.A., Kloser, R.J., Keith, G., 2015. Reducing bias due to noise and attenuation in open-ocean echo integration data. *ICES J. Mar. Sci.* 72(8): 2482-2493. doi:10.1093/icesjms/fsv121
- Schlitzer, R., 2013. Ocean Data View, <http://odv.awi.de>
- Singh, A., Gandhi, N., Ramesh, R., Prakash, S., 2015. Role of cyclonic eddy in enhancing primary and new production in the Bay of Bengal. *J. Sea Res.* 97: 5–13. <https://doi.org/10.1016/j.seares.2014.12.002>
- Torgersen, T., Kaartvedt, S., 2001. *In situ* swimming behaviour of individual mesopelagic fish studied by split-beam echo target tracking. *ICES J. Mar. Sci.* 58: 346-354. doi:10.1006/jmsc.2000.1016
- Trenkel, V.M., Berger, L., Bourguignon, S., Doray, M., Fablet, R., Massé, J., Mazauric, V., Poncelet, C., Quemener, G., Scalabrin, C., Villalobos, H., 2009. Overview of recent progress in fisheries acoustics made by Ifremer with examples from the Bay of Biscay. *Aquat. Living Resour.* 22: 433-445. doi: 10.1051/alr/2009027
- Vianello, P., Herbertte, S., Ternon, J-F., Demarcq, H., Roberts, M., 2020. Circulation and hydrography in the vicinity of a shallow seamount on the northern Madagascar Ridge. *Deep Sea Res. Part II.*
- Watanabe, H., Kawaguchi, K., Hayashi, A., 2002. Feeding habits of juvenile surface migratory myctophid fishes (family Myctophidae) in the Kuroshio region of the western North Pacific. *Mar. Ecol. Prog. Ser.* 236: 263–272. <https://doi.org/10.3354/meps236263>
- Weiss, J., 1991. The dynamics of enstrophy transfer in two-dimensional hydrodynamics. *Physica D: Nonlinear Phenomena.* 48: 273–294.
- White, M., Bashmachnikov, I., Arstegui, J., Martins, A., 2007. Physical Processes and Seamount Productivity, in: Pitcher, T.J., Morato, T., Hart, P.J.B., Clark, M.R., Haggan, N., Santos, R.S. (Eds.), *Seamounts: Ecology, Fisheries & Conservation.* Blackwell Publishing Ltd, Oxford, UK, pp. 62–84. <https://doi.org/10.1002/9780470691953.ch4>
- Wilson, C.D., Boehlert, G.W., 2004. Interaction of ocean currents and resident micronekton at a seamount in the central North Pacific. *J. Mar. Syst.* 50: 39–60. <https://doi.org/10.1016/j.jmarsys.2003.09.013>

List of figures:

Figure 1(a) Map of MAD-Ridge and La Pérouse CTD stations (diamond symbols) conducted in the East African Coastal (EAFR) and Indian South Subtropical Gyre (ISSG) provinces respectively. Longhurst's (2007) biogeochemical provinces are delimited by black solid lines. Landmasses are shown in grey and seamount summits in red. (b) La Pérouse CTD stations are plotted on the bathymetry (m). The colour bar represents the depth (m) below the sea surface.

Figure 2 Satellite surface absolute dynamic height (m) on 19 November 2016 during MAD-Ridge cruise. Geostrophic velocity vectors (m s^{-1}) (black arrows) and the position of CTD stations numbered 1-31 (grey dots) are superimposed along the West-East (W-E) and South-North (S-N) transects. Madagascan landmass is shown in orange.

Figure 3 Vertical distributions of (a) current speed (cm s^{-1}), (b) temperature ($^{\circ}\text{C}$), and (c) chlorophyll *a* (mg m^{-3}) for MAD-Ridge Leg 1 West-East transect (CTD stations labelled 1-15, left panels) across the cyclonic (C) and anticyclonic (AC) eddies, and South-North transect (CTD stations labelled 16-31, right panels) across the anticyclonic eddy and shelf (Sf). The MAD-Ridge seamount and the Madagascan shelf are shown in grey.

Figure 4 West-East (W-E) transect of MAD-Ridge: Mean micronekton acoustic density (s_A , $\text{m}^2 \text{nmi}^{-2}$) from Day_I to Day_V and Night_I to Night_IV: grey for surface layer (10-200 m), white for intermediate layer (200-400 m) and black for deep layer (400-735 m). Stacked bars are labelled: C (Cyclonic), C/D.I (Cyclonic/Dipole Interface), S/AC (Summit/ Anticyclonic), AC (Anticyclonic), AC/P (Anticyclonic/ Eddy periphery) and D.I (Dipole Interface).

Figure 5 Echogram of the 38 kHz frequency across CTD stations 6-8 (denoted by striped bars). Deep topographic features X and Y and MAD-Ridge seamount are labelled in red. Periods corresponding to sunset, night, sunrise and day are denoted by red, blue, violet and gold horizontal rectangles, respectively. Colour bar indicates s_A in $\text{m}^2 \text{nmi}^{-2}$.

Figure 6 RGB composite images of S_V values ($\text{dB re } 1 \text{ m}^{-1}$) across cyclonic CTD stations 2-3 and 4 and anticyclonic stations 10-12 and stations 13-15 (denoted by striped bars). The 38, 70 and 120 kHz frequencies were given red, green and blue colour codes, respectively, as explained in the methods. Periods corresponding to sunset, night, sunrise and day are denoted by red, blue, violet and gold horizontal rectangles, respectively.

Figure 7 South-North (S-N) transect of MAD-Ridge: Mean micronekton acoustic density (s_A , $\text{m}^2 \text{nmi}^{-2}$) from Day_VI to Day_X and Night_VI to Night_IX: grey for surface layer (10-200 m), white for intermediate layer (200-400 m) and black for deep layer (400-735 m). Stacked bars are labelled: AC (Anticyclonic), AC/F/S (Anticyclonic/Flank/Summit), S/F/AC (Summit/Flank/Anticyclonic), AC/P (Anticyclonic/Eddy periphery) and AC.P/S (Anticyclonic eddy periphery and shelf), S/AC (Summit/Anticyclonic) and AC.P (Anticyclonic eddy periphery).

Figure 8 RGB composite images of S_V values ($\text{dB re } 1 \text{ m}^{-1}$) at anticyclonic CTD stations 21-23 and shelf stations 30-31 (labelled by striped bars). The 38, 70 and 120 kHz frequencies were given red, green and blue colour codes respectively. Periods corresponding to sunset, night, sunrise and day are denoted by red, blue, violet and gold horizontal rectangles, respectively.

Figure 9(a) Boxplots of total micronekton acoustic densities (s_A , $m^2 \text{ nmi}^{-2}$) of the 38 kHz frequency in the deep (400-735 m), intermediate (200-400 m), surface layers (10-200 m) and total water column (10-735 m) for the transects at CTD stations: 10-13, 16-19, 24, 25 (AC: anticyclonic); 2, 3, 4 (C: cyclonic); 5 (Dipole Interface); 7, 9, 20, 23 (Flank/AC); 30, 31 (Shelf); and 8, 21, 22 (Summit/AC) of the MAD-Ridge cruise. Mean and standard deviations of the variables (b) SLA (m), (c) Temperature at 100 m, (d) Fmax depth (m), (e) integrated chlorophyll *a* between 2-200 m (mg m^{-3}), and (f) zooplankton biovolume ($\text{mm}^3 \text{ m}^{-3}$) are plotted for the AC, C, Dipole I., Flank/AC, Shelf and Summit/AC stations.

Figure 10 Satellite surface absolute dynamic height (m) on 16 September 2016 during the La Pérouse cruise showing La Pérouse seamount (black star). Geostrophic velocity vectors (m s^{-1}) (black arrows) are superimposed. Réunion landmass is shown in orange.

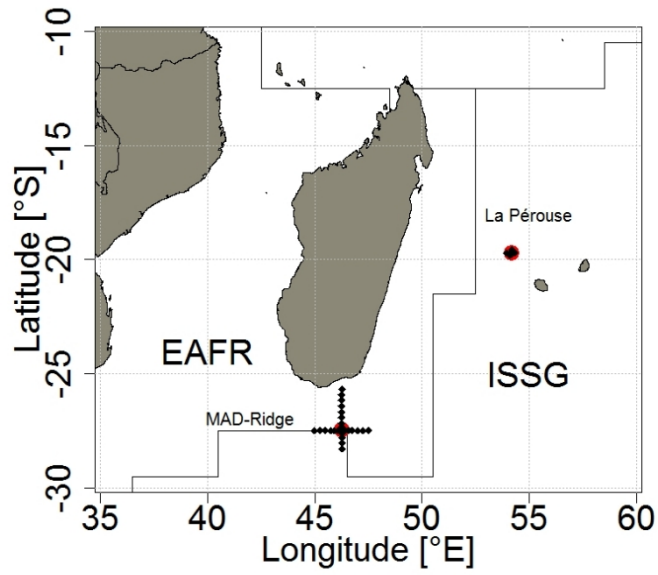
Figure 11 Map of La Pérouse and MAD-Ridge, daytime (yellow lines) and night-time (blue lines) acoustic transects plotted on the bathymetry. Colour bar indicates bathymetry (m) and the scale bar is given. Bar charts of mean micronekton acoustic densities (s_A , $m^2 \text{ nmi}^{-2}$) \pm standard deviations during the day and night: grey for surface layer (10-200 m), white for intermediate layer (200-400 m) and black for deep layer (400-735 m) at (a) La Pérouse and (b) MAD-Ridge.

Figure 12 RGB composite images of S_V values ($\text{dB re } 1 \text{ m}^{-1}$) of (a) La Pérouse day, (b) MAD-Ridge day, (c) La Pérouse night and (d) MAD-Ridge night. The MAD-Ridge and La Pérouse summits are shown in black. The 38, 70 and 120 kHz frequencies were given red, green and blue colour codes, respectively. Regions of high S_V are denoted by “white patches” on the RGB composites.

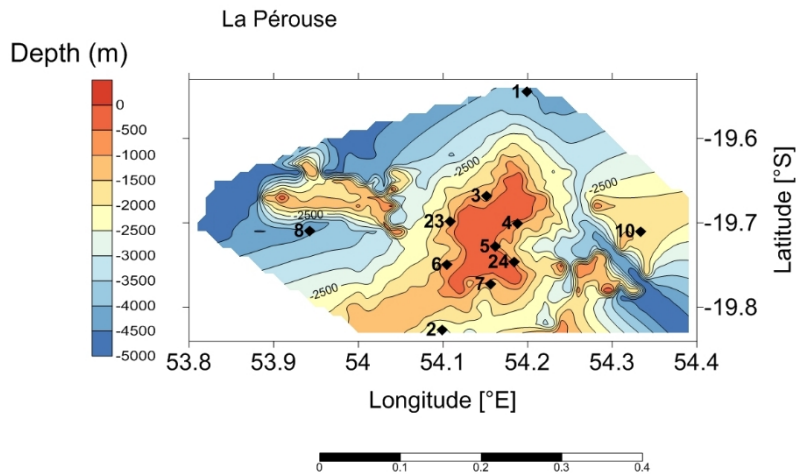
Table 1 List of MAD-Ridge Leg 1 classified hydrographic stations: UN for unresolved; C for Cyclonic; D.I for Dipole Interface; AC for Anticyclonic; S for summit; F for flank; Sf for Shelf.

Station Number	Day/ Sunset	ADT (m)	MSLA (m)	Vorticity (s ⁻¹)	Okubo-Weiss (s ⁻²)	Temperature (°S) TSG	Salinity (PSU) TSG	Sea floor Depth (m)	Classifications
1	Day	0.89	-0.19	-1.21E-05	1.63E-11	23.68	35.36	1573	UN
2	Day	0.82	-0.27	-1.97E-05	5.00E-11	23.92	35.36	1930	C
3	Sunset	0.84	-0.25	-2.94E-05	-5.32E-10	23.89	35.38	1630	C
4	Day	0.96	-0.15	-1.50E-05	-4.97E-10	23.72	35.30	1730	C
5	Day	1.08	-0.03	-5.80E-07	1.02E-10	24.37	35.14	1460	D.I
6	Day	1.21	0.10	1.49E-05	6.14E-11	24.71	35.18	1760	UN
7	Day	1.30	0.20	2.86E-05	-3.34E-10	24.40	35.21	670	F/AC
8	Day	1.33	0.23	3.15E-05	-4.92E-10	24.39	35.22	240	S/AC
9	Day	1.36	0.25	3.14E-05	-5.33E-10	24.33	35.22	645	F/AC
10	Day	1.42	0.32	3.01E-05	-5.85E-10	24.31	35.28	1600	AC
11	Day	1.46	0.36	2.86E-05	-6.71E-10	24.49	35.28	1733	AC
12	Day	1.45	0.37	2.54E-05	-5.62E-10	24.55	35.29	1585	AC
13	Day	1.41	0.35	2.55E-05	-6.09E-10	24.42	35.28	1505	AC
14	Day	1.31	0.27	1.81E-05	-3.23E-10	24.40	35.23	1964	UN
15	Day	1.18	0.16	6.75E-07	7.35E-11	24.79	35.28	2110	UN
16	Day	1.25	0.22	1.94E-05	-2.80E-10	24.25	35.21	1927	AC
17	Day	1.34	0.28	1.95E-05	-2.20E-10	24.57	35.29	2380	AC
18	Sunset	1.41	0.32	2.44E-05	-3.40E-10	24.58	35.28	1674	AC
19	Day	1.43	0.33	2.69E-05	-4.79E-10	24.38	35.22	1668	AC
20	Day	1.41	0.31	2.76E-05	-4.98E-10	24.65	35.23	720	F/AC
21	Day	1.4	0.30	2.77E-05	-5.06E-10	24.84	35.24	257	S/AC
22	Day	1.41	0.30	2.63E-05	-4.58E-10	24.40	35.24	255	S/AC
23	Day	1.41	0.30	2.58E-05	-4.32E-10	24.77	35.24	621	F/AC
24	Day	1.4	0.28	2.42E-05	-3.50E-10	24.77	35.24	1502	AC
25	Day	1.38	0.27	2.22E-05	-2.12E-10	24.77	35.24	1585	AC
26	Day	1.32	0.22	1.50E-05	1.14E-11	24.46	35.14	1747	UN
27	Day	1.25	0.20	8.21E-06	1.09E-12	24.46	35.14	1916	UN
28	Day	1.21	0.23	9.75E-06	-9.40E-11	24.47	35.14	2125	UN
29	Day	1.11	0.23	2.25E-06	3.08E-11	24.73	35.15	1875	UN
30	Day	1.00	0.21	-7.82E-06	7.21E-11	24.77	35.21	1436	Sf
31	Sunset	0.95	0.19	-7.39E-06	1.82E-10	24.68	35.30	840	Sf

a)



b)



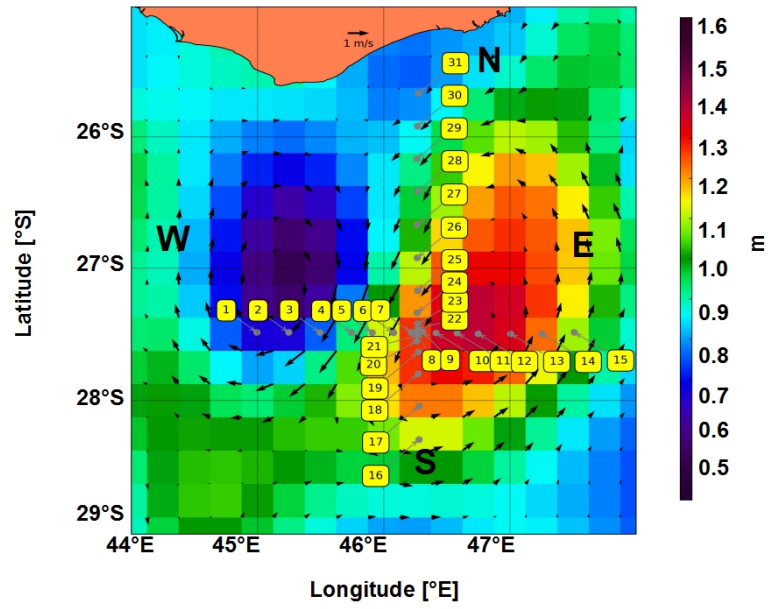


Figure 2

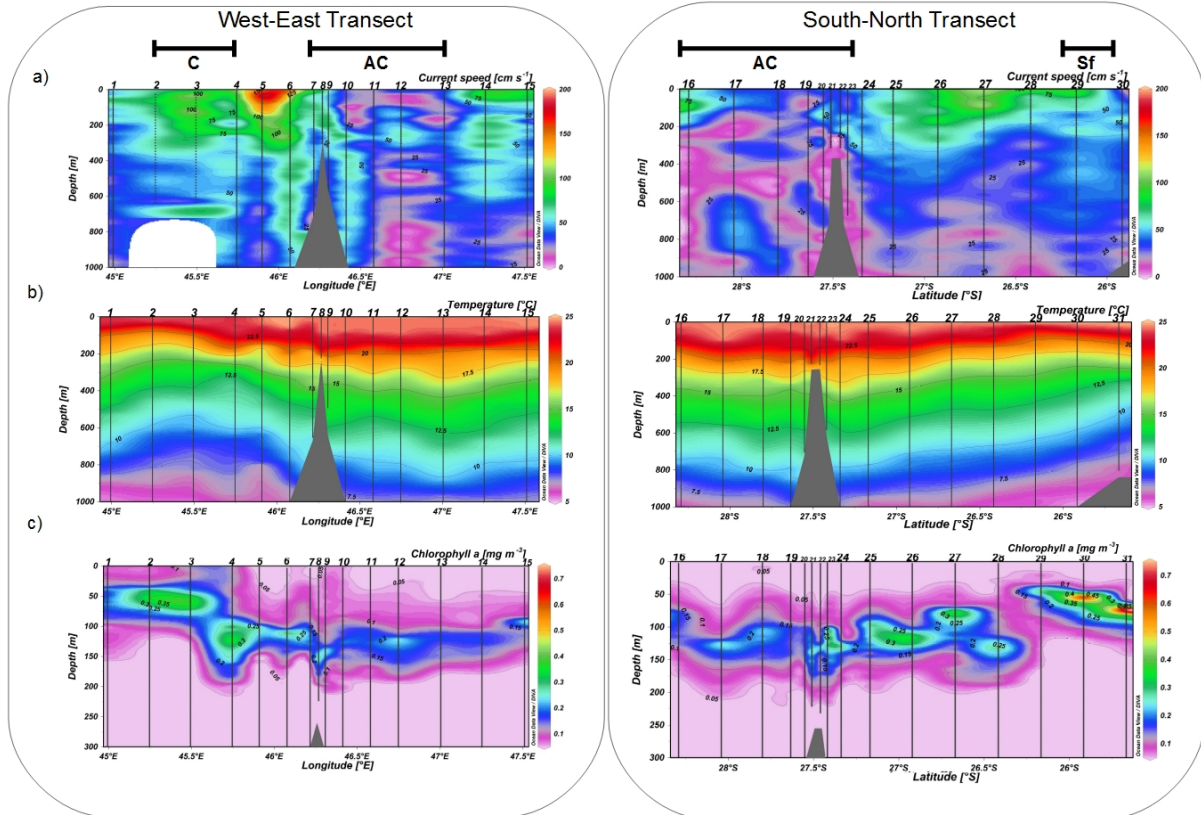


Figure 3

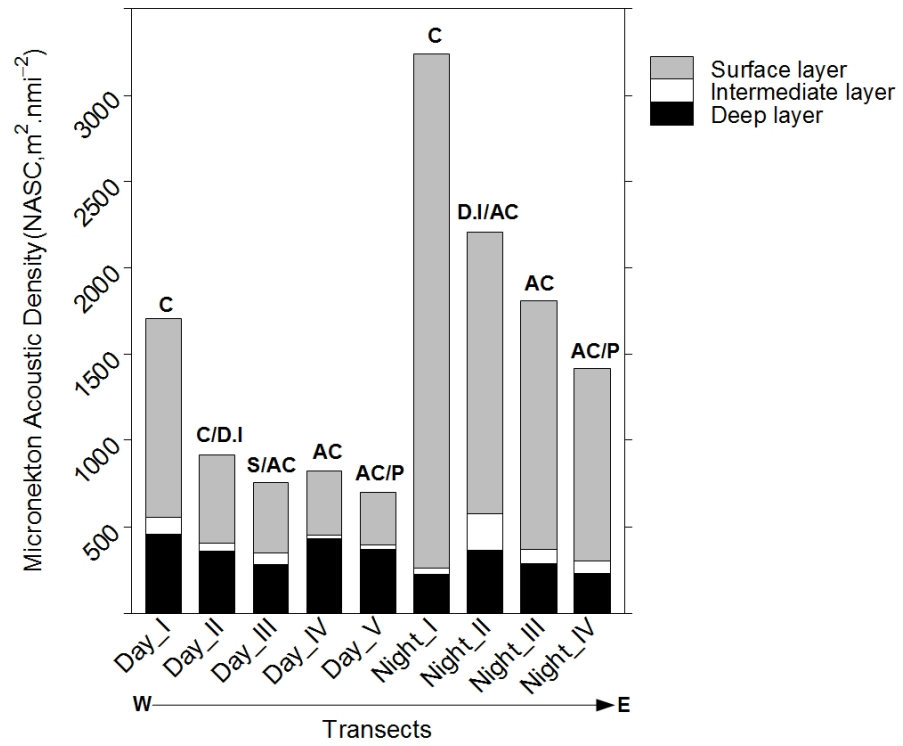


Figure 4

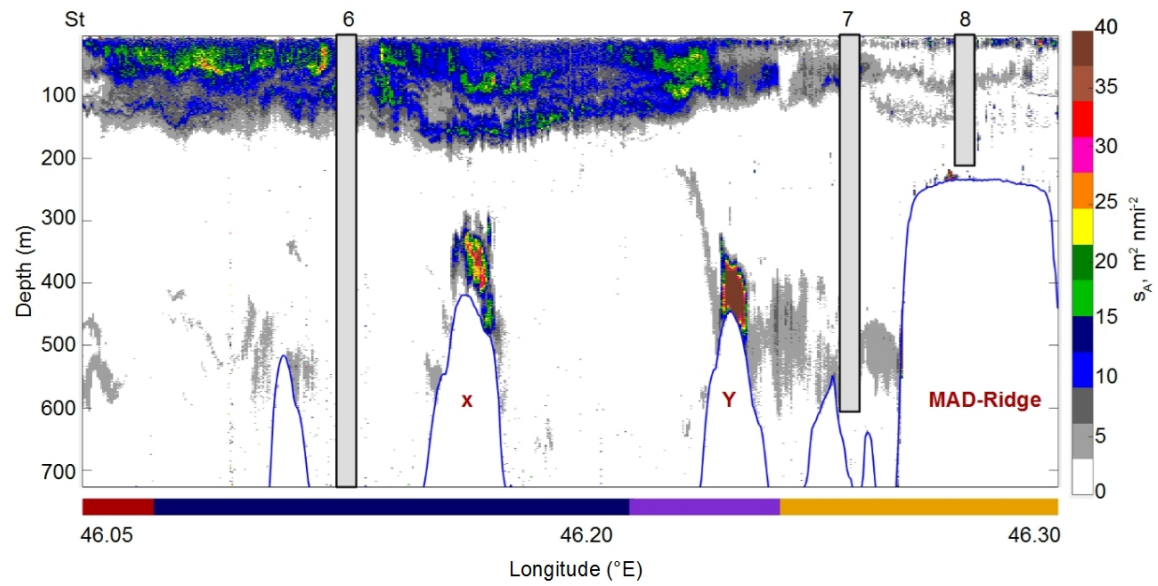


Figure 5

Red: Sv 38 kHz; Green: Sv 70 kHz; Blue: Sv 120 kHz

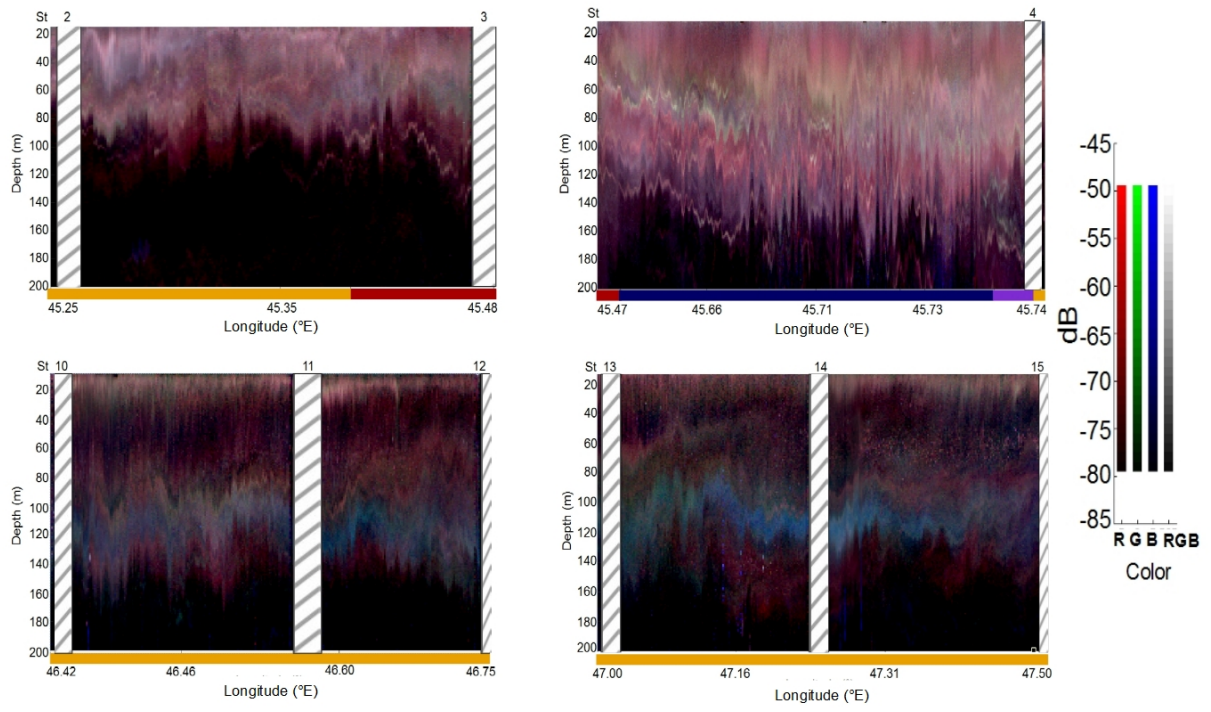


Figure 6

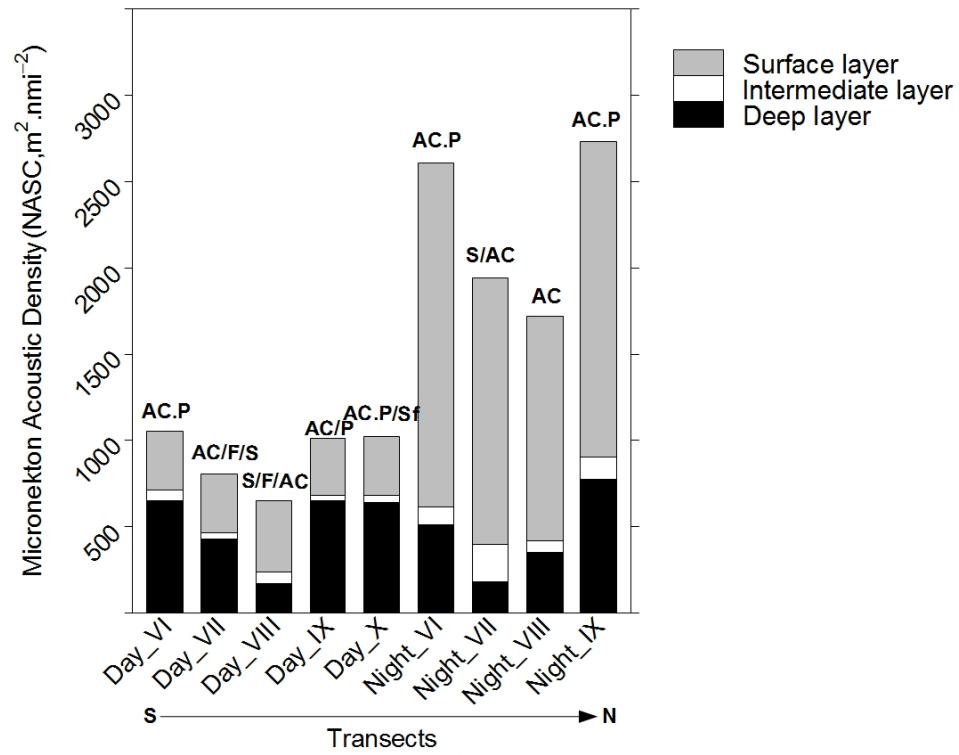


Figure 7

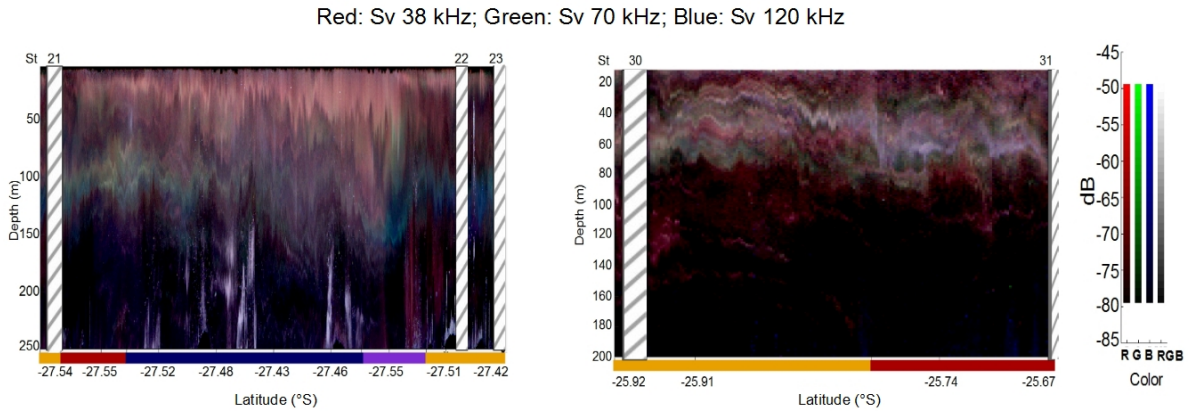


Figure 8

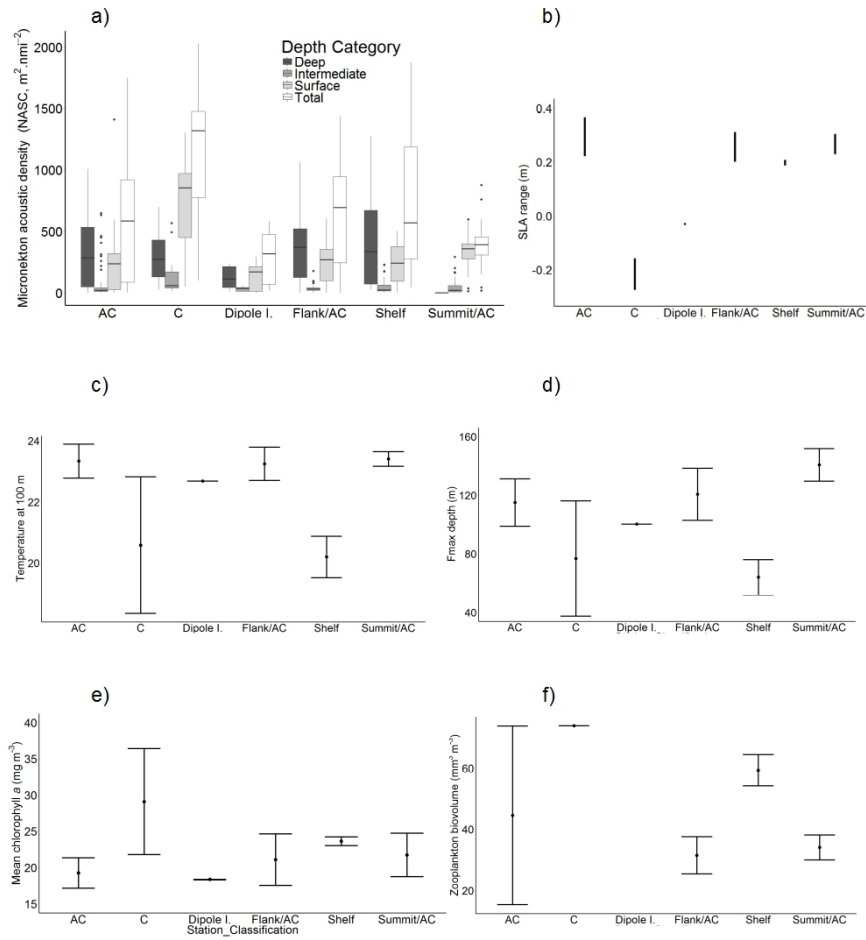


Figure 9

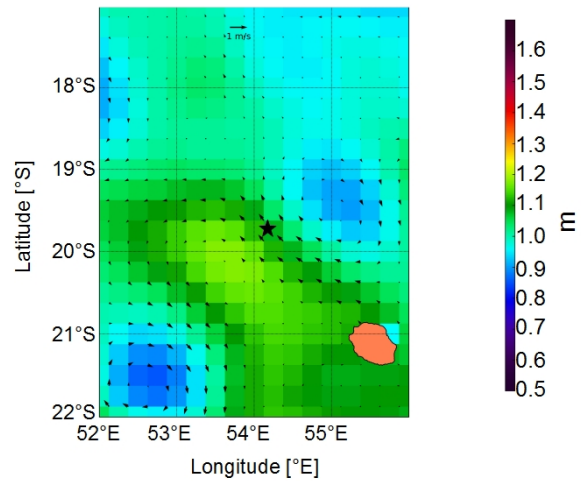


Figure 10

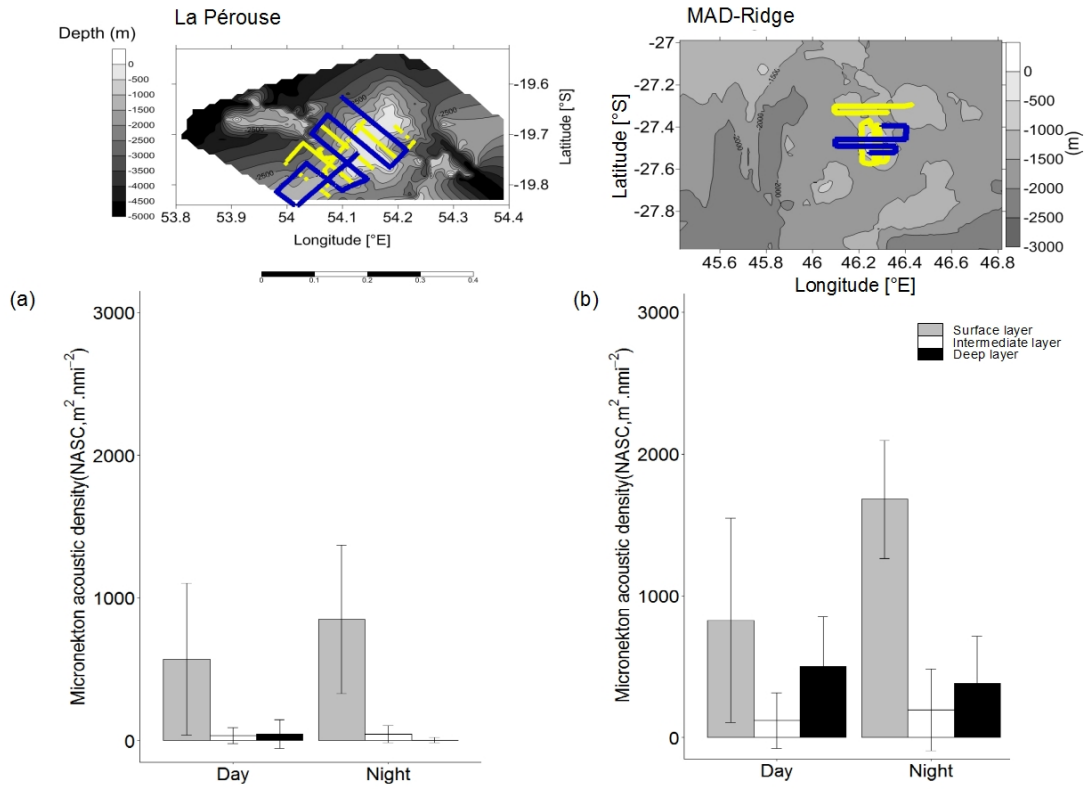
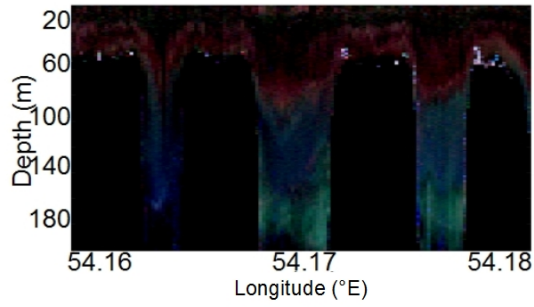


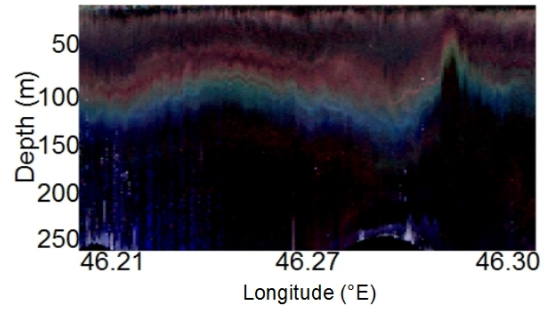
Figure 11

Red: 38 kHz; Green: 70 kHz; Blue: 120 kHz

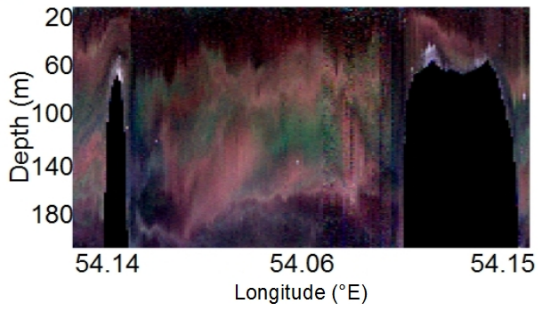
(a) La Pérouse Day



(b) MAD-Ridge Day



(c) La Pérouse Night



(d) MAD-Ridge Night

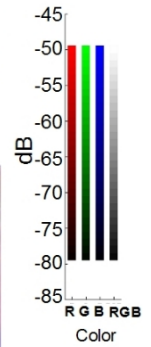
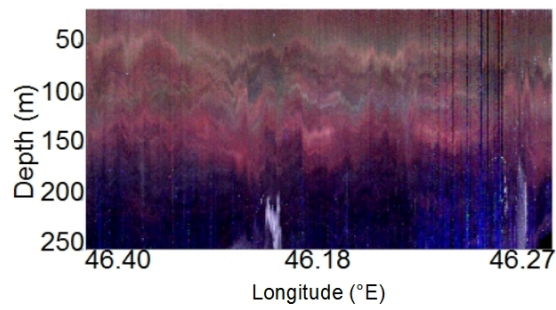


Figure 12